

Article

Characteristics of Clouds and Raindrop Size Distribution in Xinjiang, Using Cloud Radar Datasets and a Disdrometer

Yong Zeng ^{1,2,*}, Lianmei Yang ^{1,2}, Zuyi Zhang ^{1,2}, Zepeng Tong ^{1,2}, Jiangang Li ^{1,2}, Fan Liu ^{1,2}, Jinru Zhang ^{1,2} and Yufei Jiang ^{1,2}

¹ Institute of Desert Meteorology, China Meteorological Administration, Urumqi 830002, China; yanglm@idm.cn (L.Y.); zhangzy@idm.cn (Z.Z.); tongzp@idm.cn (Z.T.); lijg@idm.cn (J.L.); liufan@idm.cn (F.L.); zhangjr@idm.cn (J.Z.); jiangyf@idm.cn (Y.J.)

² Center for Central Asian Atmosphere Science Research, Urumqi 830002, China

* Correspondence: zengyong@idm.cn

Received: 30 November 2020; Accepted: 17 December 2020; Published: 21 December 2020



Abstract: Observation data from March to May 2020 of the Ka-band millimeter-wave cloud radar and disdrometer, located in Xinjiang, a typical arid region of China, were used to study the diurnal variation of clouds and precipitation, raindrop size distribution (DSD), and the physical parameters of raindrops. The results showed that there are conspicuous diurnal changes in clouds and precipitation. There is a decreasing trend of the cloud base height (CBH) from 05:00 to 19:00 CST (China Standard Time, UTC +8) and a rising trend of CBHs from 20:00 to 04:00 CST. The cloud top height (CTH) and the cloud thickness show a rising trend from 03:00 to 05:00 CST, 12:00 to 14:00 CST, and 20:00 to 01:00 CST. The diurnal variation of clouds is mainly driven by wind and temperature closely related to the topography of the study area. There are three apparent precipitation periods during the day, namely, 02:00–09:00 CST, 12:00 CST, and 17:00–21:00 CST. The changes in the physical parameters of raindrops are more drastic and evident with a lower CBH, lower CTH, and higher number of cloud layers from 12:00 to 21:00 CST than other times, which are closely related to day-to-day variations of systems moving through, and incoming solar radiation and the mountain–valley wind circulation caused by the trumpet-shaped topography that opens to the west played a secondary role. The DSD is in agreement with a normalized gamma distribution, and the value of the shape factor μ is significantly different from the fixed μ value in the Weather Research and Forecasting (WRF) Model. The rain in arid Xinjiang had a higher concentration of raindrops and a smaller average raindrop diameter than the rain in other humid regions of the Central and Southeast Asian continent. In the $Z - R$ (radar reflectivity–rain rate) relationship, $Z = 249R^{1.20}$ is derived for stratiform rain, and it is significantly different from humid regions. Using Z/D_m (mass-weighted mean diameter) and R , a new empirical relationship $Z/D_m = 214R^{1.20}$ is established, and improvement is obtained in rain retrieval by using the $Z/D_m - R$ relation relative to the conventional $Z - R$ relation. Additionally, the $N_t - R$, $D_m - R$, $N_w - R$, and $N_t - N_w$ relationships with larger differences from humid regions are established by fitting the power-law equations. These results are useful for improving the data parameters of microphysical processes of WRF and the accuracy of quantitative precipitation estimation in arid regions.

Keywords: clouds and precipitation; cloud radar; disdrometer; arid area; raindrop size distribution

1. Introduction

Cloudiness is one of the key factors affecting climate change, and it plays an important role in the radiation budget, energy balance, and water cycle of the Earth's atmosphere [1–4]. The climate effect of

cloud radiation strongly depends on the macro- and microphysical properties of the cloud. Therefore, the observation, inversion, and research on the macroscopic and microscopic physical properties of clouds are important for improving the parameterization processing of clouds in the Weather Research and Forecasting (WRF) Model and to understand the feedback effect of clouds in climate change [5–7].

At present, the macro- and microphysical characteristics of clouds are mainly observed and studied by ground-based equipment, aircraft, and satellites [8–10]. Aircraft can obtain the vertical characteristics of clouds by completing multiple passes at different altitudes [11,12]. However, it is expensive, and clouds can only be observed for a brief time and at a specific location [13]. Satellite observations can obtain the characteristic distribution of clouds on a regional and global scale, but the temporal and spatial resolution is low, and the accuracy and reliability of the results need to be verified by ground-based observations [14–16]. Ground-based detection has high time resolution and inversion accuracy and can be used for continuous observation of an area. The wavelength emitted by the millimeter-wave cloud radar (MMCR) in ground-based detection belongs to the millimeter-wave band and has strong cloud penetrability. It can observe high-level cirrus clouds through low-level water clouds and detect the vertical structure of multi-layer clouds. Additionally, MMCR can obtain clouds' macro- and micro-vertical structure and cloud phase information through products such as reflectance factor, Doppler velocity, and depolarization ratio profile, and then can invert cloud microphysical properties. Therefore, MMCR is a powerful tool for studying the macro- and micro-properties of clouds [17–19]. Liu et al. [20] studied the day–night cycle and vertical structure of clouds using MMCR in South China, one of the most humid regions of mainland China, with a tropical–subtropical climate that includes Guangdong Province, the Guangxi Zhuang Autonomous Region, Hainan Province, the Hong Kong Special Administrative Region and the Macau Special Administrative Region. Liu et al. [20] proposed that numerous clouds are distributed below 3 km and are most prominent at sunrise, noon, and sunset. Zheng et al. [21] investigated warm clouds by MMCR in South China during the pre-flood season and found that warm clouds are mainly distributed at altitudes below 2.5 km, and the height of the cloud base, height of the cloud top, and cloud thickness have the characteristics of a diurnal variation. However, research on cloud characteristics and diurnal changes in arid areas using radar is limited.

Raindrop size distribution (DSD) reflects the characteristics of the concentration of raindrop particles within a limited droplet size per unit volume. Raindrop spectrum research is often aimed at the microphysical process of precipitation, which is important for improving the accuracy of quantitative precipitation estimation by radar and improving and optimizing the precipitation parameterization scheme in models [22–25]. Due to the differences in climate, atmospheric conditions, and topographical conditions, DSD shows evident temporal and spatial changes [26–28]. Therefore, studying DSD is important for understanding the microphysical characteristics of different types of precipitation and improving the parameterization level of models.

At present, raindrop disdrometers, including the Particle Size and Velocity disdrometer, Joss and Waldvogel disdrometer, and the two-dimensional video disdrometer [29–31], are widely used in the continuous measurement of raindrop spectra due to their high accuracy, stability, and time resolution [32–34]. In the process of quantitative precipitation estimation (QPE), the measured raindrop spectrum can be used to calibrate and verify the parameters A and b in the power function relationship between radar reflectivity and rainfall intensity ($Z = AR^b$) [35–37]. Atlas et al. [38] calculated the relationship between A and b in the $Z - R$ relationship of different precipitation processes and found that A and b are inversely related. The convective precipitation observed by Maki et al. [39] led to a similar conclusion with Atlas et al. [38], but A remained constant and is independent of b in the stratiform cloud system. Reddy and Kozu [40] pointed out that the $Z - R$ relationship and DSD in the control of different monsoon systems are different. Sharma et al. [41] proposed that by using the $Z/D_m - R$ relationship relative to the conventional $Z - R$ relationship, the accuracy of rain intensity estimation is significantly improved. Wu et al. [42] compared A and b in the $Z-R$ relationship between the Qinghai–Tibet Plateau and southern China and pointed out that A is larger, and b is smaller in

southern China. Wen et al. [43] proposed that the coefficient A and the index b in the Z–R relationship obtained by fitting are different in the four seasons in eastern China. Simultaneously, the WRF model is a valuable tool for precipitation forecasting or simulation, and DSD model parameters in the WRF model are mainly determined by the microphysics parameterization setting [44]. Many studies have highlighted the sensitivity of WRF forecasts to the choice of microphysics, and successfully evaluated QPE in model [45–47]. Gilmore et al. [48] illustrated the impact of different DSDs on the variation in rainfall accumulations and showed great ambiguities in the modeled outputs. Thus, the DSD model, which depends on the choice of microphysics schemes and particle parametric variables, is extremely important for the accuracy and uncertainty of QPE in model [44]. However, there are few studies on the DSD and Z–R relationship in arid areas using a disdrometer.

Xinjiang is in northwestern China comprising about one-sixth of the total land area of China and has a typical arid climate. Unlike central and eastern China, Xinjiang is not directly affected by the monsoon system and has less overall precipitation [49–51]. The Tianshan Mountains in Central Xinjiang are the most important mountains in the region and are distributed in a quasi-east–west direction with a maximum altitude of more than 5000 m. The area nearest the Tianshan Mountains is where the primary human occupation occurs and where the majority of precipitation occurs, while the famous Taklimakan Desert and the Gurbantungut Desert are distributed on the north and south regions opposite the Tianshan Mountains, with scarce precipitation. From the global atmospheric circulation perspective, Xinjiang is in a westerly flow belt area and precipitation is associated with the presence of troughs and vortices moving eastward in the westerly belt throughout the year. So, clouds and precipitation are extremely important to the ecological environment and life in this arid area.

Xinjiang is one of the most important agricultural and animal husbandry regions in China. Spring rainfall is crucial for the planting and growth of crops and grasslands, thereby affecting the food security of China. However, the skill of precipitation forecasting in this area is low, especially when the weaker influence system moves to areas near the mountains, the forecast accuracy of the precipitation process is relatively lower. [52,53]. There are three primary reasons for this: the first reason is that the various microphysical parameterization schemes developed in the numerical model do not match in this area. Specifically, the microphysical parameterization schemes used in the WRF in rainfall forecasting of Xinjiang are the double-moment 6-class (WDM6) scheme [54] and the Thompson aerosol-aware scheme [55], both of which are second-order schemes, that is, assuming that the shape factor μ is a fixed value of 0 and 1, respectively, which are obviously inconsistent with reality. Therefore, it is necessary to obtain the local μ value through observation to improve the rainfall simulation results. The second reason is the lack of localized microphysical research in Xinjiang. In the past, due to the scarcity of observation equipment, the research on microphysics was very lacking, which was mainly caused by the underdeveloped local economy in the past. The third reason is the extremely complex terrain and sparse weather stations in the area [56]. The habitable areas and major cities in Xinjiang are near the mountains. However, the meteorological observation stations near the mountains are sparse, and the meteorological observation stations in Central Asia (such as Kazakhstan, Kyrgyzstan, etc.) in the western part of Xinjiang are even rarer, and the local economy is relatively backward compared to the central and eastern regions of China, so past studies have paid less attention to this region. The reason for the poor precipitation forecast in this area also includes that the Doppler weather radar is seriously blocked by the terrain during the scanning process, and the satellites are mainly located in the sky over eastern China, so there is a certain deviation in the projection to Xinjiang. In addition, it also includes the lack of research on the gravity waves excited by the terrain, and the difference between the underlying surface in the WRF and the actual one, etc. Unclear microphysical characteristics also lead to a limited QPE accuracy. Simultaneously, the detection of clouds and precipitation using MMCR and disdrometer also has a key impact on the effective use of cloud water resources. Therefore, the objective of this study is to reveal the microphysical characteristics of clouds and precipitation in the Xinjiang region, thereby improving the QPE in this area and improving the microphysical parameterization scheme to adapt the precipitation forecast in this area.

In this study, cloud and DSD data in Xinjiang were collected in the spring of 2020, and the diurnal variation of clouds and precipitation were revealed using these data. Finally, the DSD features and QPE estimators were investigated with fitting by the moment method and the least square method, respectively. A preliminary new empirical relationship, $Z/D_m - R$ is better than the conventional $Z - R$ relationship in the QPE, and a case study also confirmed this conclusion. The remaining parts of the study are organized as follows. Section 2 introduces the instruments and data, as well as data processing, and quality control methods. The diurnal variation of clouds and precipitation, the characteristics of the raindrop spectrum, the $Z - R$ relationship, the $Z/D_m - R$ relationship, and a case study are described in detail in Section 3. Section 4 discusses the differences between the present results and previous studies. Section 5 presents the conclusions of the study.

2. Materials and Methods

2.1. Instruments and Measurements

To further understand the characteristics of clouds and precipitation in arid areas, the Institute of Desert Meteorology, China Meteorological Administration, Urumqi, conducted cloud and precipitation observation experiments in Xinjiang Province, China, from 1 March to 31 May 2020. The experiments were carried out at the Xinyuan Meteorological Station (XY, 83.25° E, 43.45° N, 929.7 m above sea level) located inside the trumpet-shaped terrain formed by the Tianshan Mountains in Xinjiang Province. Instruments included an MMCR and disdrometer. The observation location and instrument are shown in Figure 1.

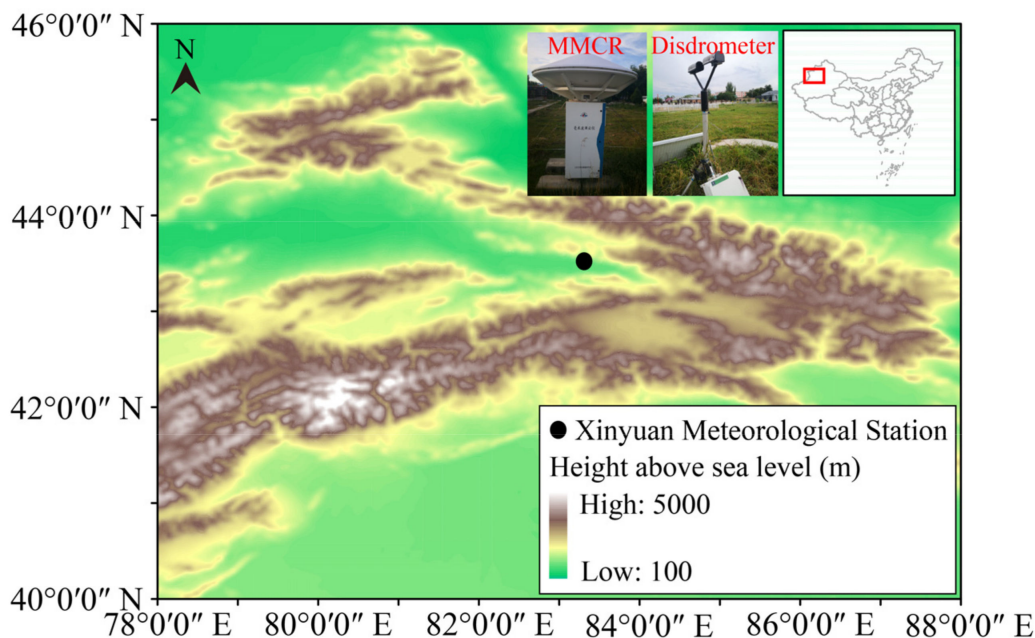


Figure 1. Location of the Xinyuan Meteorological Station (XY, 83.25° E, 43.45° N, 929.7 m above sea level) and the photos of the millimeter-wave cloud radar (MMCR) and disdrometer at the Xinyuan Meteorological Observatory.

2.1.1. Ka-Band MMCR

The MMCR used in this study was a Ka-band radar of 8 mm wavelength produced by the No. 23 Research Institute of China Aerospace Science and Industry Corporation. The Ka-band MMCR adopts an all coherent, all solid-state, pulse compression, pulse Doppler, single-shot, single polarization radar, which can obtain cloud base height (CBH), cloud top height (CTH), cloud thickness (CTK), cloud layer number (CLN), other cloud macroscopic properties, radar reflectivity, mean Doppler velocity, spectrum

width, and other microphysical characteristics. The Ka-band MMCR has a temporal resolution and spatial resolution of 1 min and 30 m, respectively, and the detection height ranges from 0.06 to 20 km. In addition to the attenuation of electromagnetic waves passing through clouds, radar noise level calculation, cloud-precipitation signal extraction, signal attenuation correction, non-meteorological echo removal, retrieval of the cloud-precipitation macrophysical quantity and other processing may also cause some uncertainty in the data [20,21].

2.1.2. Disdrometer

The disdrometer used in this study was a Particle Size and Velocity (PARSIVEL) disdrometer produced by the OTT Hydromet Company (Kempten, Germany). The disdrometer emits a 54 cm^2 laser beam every 1 min to record raindrop diameters (D) and raindrop terminal velocity (V) by measuring the signal attenuation caused by raindrops passing through the laser beam at a height of 1.4 m above the ground. D and V are divided into 32 non-equally spaced measurement channels. On this basis, information such as rainfall intensity (R), radar reflectivity (Z), and DSD can also be obtained. Previous studies indicated that the impossibility of PARSIVEL disdrometer to detect raindrops with diameters smaller than 0.2 mm may produce unreasonable results [21].

2.2. Data Processing and Quality Control (QC)

Data quality has a certain impact on the application of the MMCR and the disdrometer results, and, therefore, it is necessary to carry out data processing and quality control [21,57].

2.2.1. Ka-MMCR Data Processing and QC

The MMCR outputs are CBH, CTH, CTK, CLN. To show the characteristics of a diurnal variation, the data are processed according to an hourly distribution. At a certain cloud layer in a certain minute, CBH of 15,030 m, CTH of 20,040 m, and CTK of 5010 m are considered to be invalid data, and the invalid data at this minute were deleted. Accordingly, CLN is reduced by 1 min.

2.2.2. Disdrometer Data Processing and QC

A PARSIVEL disdrometer assumes a spherical shape of raindrops in its observations, and large raindrops deform significantly while falling, therefore, the D of raindrops needs to be corrected. This study adopts the axial ratio correction method of Battaglia et al. [58]: assuming that the raindrops with $D \leq 1 \text{ mm}$ have no deformation and the axial ratio is 1; raindrops with $1 \text{ mm} < D \leq 5 \text{ mm}$ vary linearly between 0.7 and 1; when $D > 5 \text{ mm}$, the axial ratio is 0.7. To analyze the spectrum type and distribution function of DSD, the observational data need to be converted into the concentration of raindrops per unit volume per unit size interval:

$$N(D_i) = \sum_{j=1}^{32} \frac{n_{ij}}{A_i \cdot \Delta t \cdot V_j \cdot \Delta D_i} \quad (1)$$

where $N(D_i)$ ($\text{m}^{-3} \cdot \text{mm}^{-1}$) represents the number concentration of raindrops per unit volume with diameters in the interval from D_i to $D_i + \Delta D_i$; n_{ij} is the number of raindrops within the size bin i and raindrop terminal velocity bin j ; A_i (m^{-2}) is the sampling area of the instrument; Δt (60 s) is the sampling time interval; V_j ($\text{m} \cdot \text{s}^{-1}$) represents raindrop terminal velocity of the j -th bin, and ΔD_i is the class spread of the i -th bin of the diameters of the spectra.

According to the raindrop spectrum data, some microphysical characteristic quantities can be obtained. The formulas for calculating precipitation intensity R ($\text{mm} \cdot \text{h}^{-1}$), liquid water content LWC

($\text{g} \cdot \text{m}^{-3}$), radar reflectivity Z ($\text{mm}^6 \cdot \text{m}^{-3}$), and the number concentration of total raindrops N_t (m^{-3}) are Formulas (2)–(5).

$$R = \frac{6\pi}{10^4} \sum_{i=1}^{32} \sum_{j=1}^{32} V_j \cdot N(D_i) \cdot D_i^3 \cdot \Delta D_i \quad (2)$$

$$LWC = \frac{\pi \rho_w}{6000} \sum_{i=1}^{32} N(D_i) \cdot D_i^3 \cdot \Delta D_i \quad (3)$$

$$Z = \sum_{i=1}^{32} N(D_i) \cdot D_i^6 \cdot \Delta D_i \quad (4)$$

$$N_t = \sum_{i=1}^{32} N(D_i) \cdot \Delta D_i \quad (5)$$

where ρ_w represents the density of water, which is $1.0 \text{ g} \cdot \text{cm}^{-3}$.

The n -th moment of the DSD can be expressed as follows:

$$M_n = \int_0^\infty N(D) \cdot D^n \cdot dD \quad (6)$$

In the process of solving other physical quantities, the mass-weighted mean diameter of raindrops D_m (mm) can be expressed by using the 3rd moment and 4th moment of the DSD as follows:

$$D_m = \frac{M_4}{M_3} \quad (7)$$

According to the derivation of Testud et al. [59], the normalized intercept parameter N_w ($\text{mm}^{-1} \cdot \text{m}^{-3}$) is calculated from the LWC and D_m as follows:

$$N_w = \frac{4^4}{\pi \cdot \rho_w} \cdot \frac{10^3 \cdot LWC}{D_m^4} \quad (8)$$

The three-parameter gamma distribution can better reflect the characteristics of the raindrop spectrum, which can be expressed as follows:

$$N(D) = N_0 \cdot D_\mu \cdot \exp(-\Lambda \cdot D) \quad (9)$$

where N_0 ($\text{mm}^{-1-\mu} \cdot \text{m}^{-3}$) is the intercept parameter, μ is the shape factor (dimensionless), and Λ (mm^{-1}) is the slope parameter [60].

However, these three parameters in a gamma distribution are not mutually independent; to solve the nonindependence problem of the parameters of the gamma DSD model, a normalization method has been proposed [61–63], which is given by

$$N(D) = N_w \cdot f(\mu) \cdot \left(\frac{D}{D_m} \right)^\mu \cdot \exp \left[-(4 + \mu) \frac{D}{D_m} \right] \quad (10)$$

where

$$f(\mu) = \frac{6 \cdot (4 + \mu)^{4+\mu}}{4^4 \cdot \Gamma(4 + \mu)} \quad (11)$$

In our research, the third, fourth and sixth moments of the DSD data are used to get normalized gamma distribution according to the derivation of Kozu and Nakamura [64] and Wu and Liu [65].

In the process of determining the characteristics of the diurnal variation, for each minute of data when the total number of raindrops output by the instrument is ≥ 10 and the $R \geq 0.1 \text{ mm} \cdot \text{h}^{-1}$, it is

regarded as one precipitation minute, and the rest are regarded as non-precipitation data. In the process of the classification of precipitation types, the constraint conditions are more stringent, as shown in Figure 2. Two conditions must be simultaneously met for precipitation minutes [66]: (1) the $R \geq 0.5 \text{ mm} \cdot \text{h}^{-1}$, and (2) the rainfall continuous-time $CT \geq 0.5 \text{ h}$. On this basis, for a certain time t_i , from $t_i - N_s$ to $t_i + N_s$, $R \geq 5 \text{ mm} \cdot \text{h}^{-1}$ and standard deviation $SD > 1.5 \text{ mm} \cdot \text{h}^{-1}$ are the convective rain event; $R < 5 \text{ mm} \cdot \text{h}^{-1}$ and $SD < 1.5 \text{ mm} \cdot \text{h}^{-1}$ are the stratiform rain event; otherwise considered as stratocumulus rain event [30,67]. In this study, the N_s is set to be five.

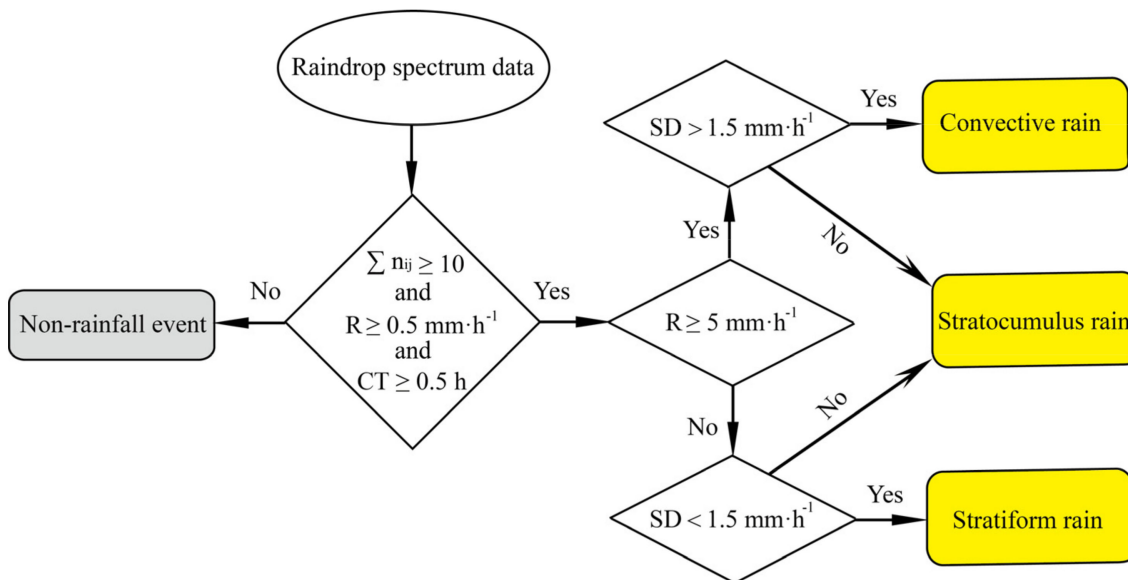


Figure 2. Flow chart of classifying stratiform, convective, stratocumulus rain, and non-rainfall.

Additionally, in the process of calculating the relationship between the two physical quantities, the correlation coefficient (CC) and root mean squared error (RMSE) are also used, and expressed as follows:

$$CC = \frac{\sum_{i=1}^n (x_i - \bar{x})(y_i - \bar{y})}{\sqrt{\sum_{i=1}^n (x_i - \bar{x})^2 \sum_{i=1}^n (y_i - \bar{y})^2}} \quad (12)$$

$$RMSE = \sqrt{\frac{1}{n} \sum_{i=1}^n (x_i - y_i)^2} \quad (13)$$

where $\bar{x} = \frac{1}{n} \sum_{i=1}^n x_i$, $\bar{y} = \frac{1}{n} \sum_{i=1}^n y_i$, n is the sample size, and x_i and y_i are two physical quantities, respectively.

3. Results

In the following subsections, the diurnal variation of clouds and precipitation were investigated in detail. Subsequently, the DSD characteristics and empirical relationships of rainfall physical quantities for precipitation in Xinjiang are proposed.

3.1. Diurnal Variation of Clouds and Precipitation

The detection and study of diurnal variation of clouds and precipitation are valuable for improving our understanding of the related physical and dynamic issues of clouds [21]. The diurnal variation of clouds and precipitation in areas with complex terrain are obvious, which are of great significance for understanding the generation and development process of clouds and rainfall [68]. To obtain a

better understanding of the diurnal variation of clouds and precipitation, in this subsection, the diurnal variation of clouds and precipitation are analyzed. Figure 3 shows the diurnal variation of the CBH, CTH, CTK, and CLN derived from Ka-band MMCR during the measurement period. Fifty percent of CBHs (Figure 3a) over 24 h varied from 60 to 2075 m, with evident diurnal characteristics. There was a decreasing trend of CBHs from 05:00 CST (China Standard Time, UTC +8) to 19:00 CST; it should be noted that the local solar time of Xinyuan is 2.5 h later than CST, and the decrease was the most significant at 10:00 CST, an increasing trend of CBHs was recorded from 20:00 CST to 04:00 CST, and the increase was the most significant at 01:00 CST. The mean CBHs also had similar diurnal variation ranging from 632 to 2712 m. Fifty percent of the CTHs and the mean CTHs (Figure 3b) over 24 h varied from 4350 to 7715 m and from 4502 to 7339 m, respectively. The CTHs over 24 h show a rising trend from 03:00 to 05:00, 12:00 to 14:00, and 20:00 to 01:00 CST, and the rest of the time showed a decreasing trend. More importantly, 75% of the total sample of CTHs were above 5000 m from 00:00 to 09:00 CST; however, there was also a large number of cloud tops at heights below 3 km from 10:00 to 23:00 CST, and the turning times of the change were 10:00 CST and 00:00 CST, respectively. Over 24 h, 50% of the CTKs and the mean CTKs (Figure 3c) show the characteristics of a diurnal variation similar to the CTHs that varied from 1770 to 5181 m and from 3269 to 4837 m, respectively. It is evident from the frequency distribution of the CTKs (Figure 3d) that the CTKs uniformly appear in the range of 1–10 km from 00:00 to 09:00 CST over 24 h, whereas the CTKs less than 2 km significantly increased from 10:00 to 23:00 CST. The frequency distribution of the CLNs (Figure 3e) over 24 h shows that the higher the CLNs, the smaller the frequency of the CLNs, and the frequency of CLNs between 10:00 and 23:00 CST is greater than the remaining period.

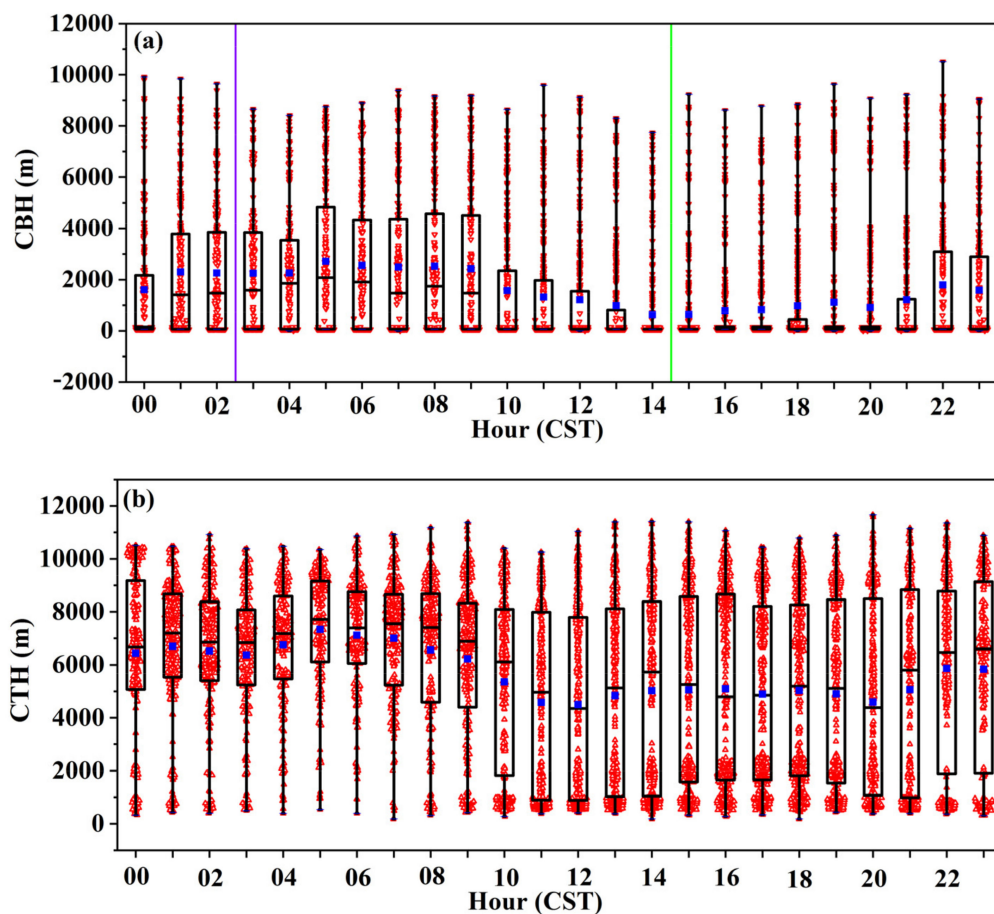


Figure 3. Cont.

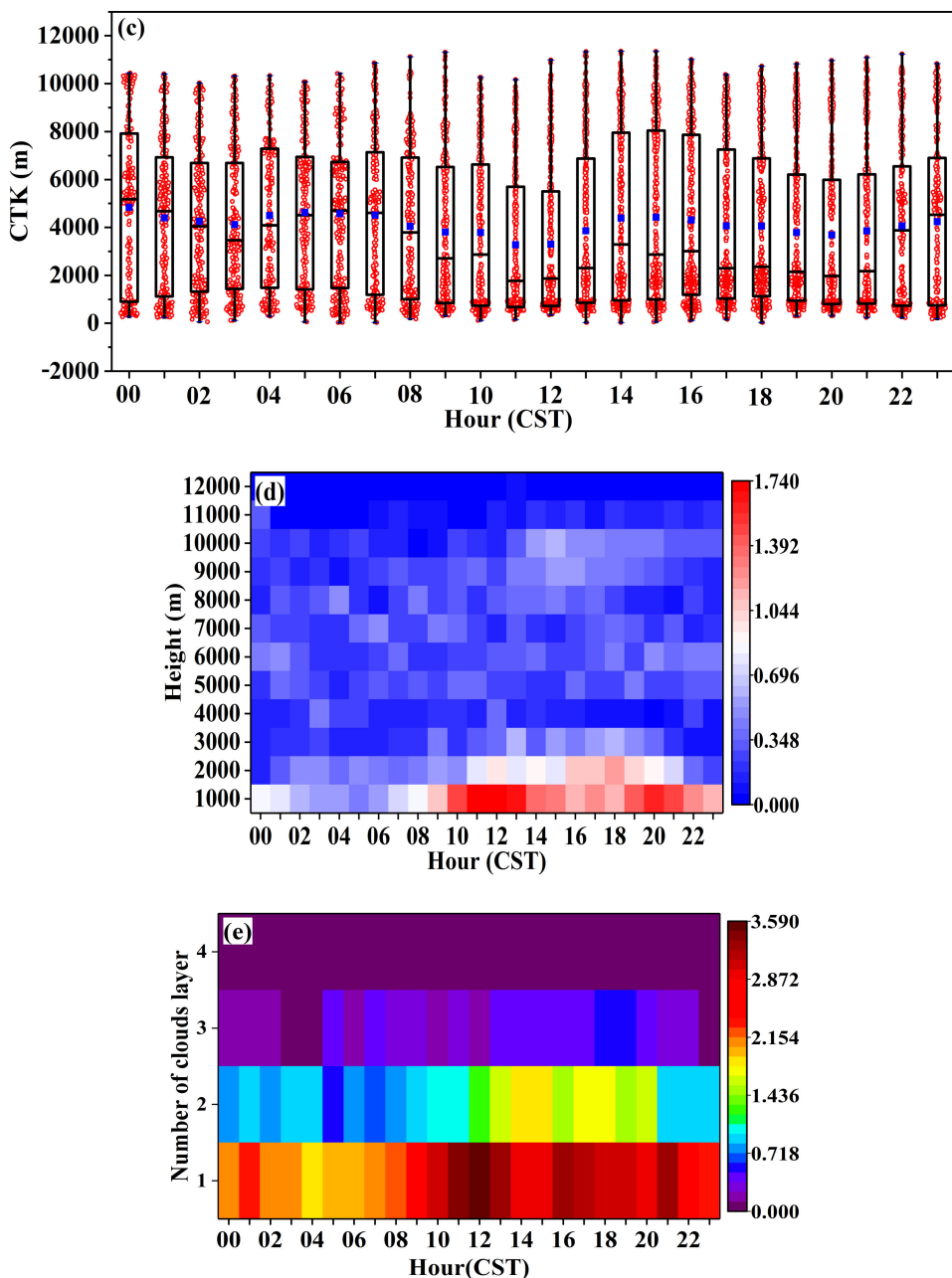


Figure 3. Diurnal variations in (a) the cloud base height (CBH) (m), (b) the cloud top height (CTH) (m), (c) the cloud thickness (CTK) (m), (d) the frequency distribution of the CTK, and (e) the frequency distribution of the cloud layer number (CLN) during the observation period. On each box, the blue square represents the average, the central crossbar indicates the median, and the bottom and top edges of the box indicate the 25th and 75th percentiles, respectively. The black whiskers extend to the maximum and minimum of the data points, respectively. The positions of the purple and green vertical lines are midday and midnight in Figure 3a, respectively.

Figure 4 shows the diurnal variations of accumulated rain amount, accumulated rainy minute number, R , N_t , D_m , N_w , Z , and LWC over a 24 h period. Figure 4a,b shows that there are three apparent precipitation periods, which are from 02:00 to 09:00, 12:00 and from 17:00 to 21:00 CST. The three periods produced maximum precipitation amounts accounting for 79.18% of the total rainfall and a higher rainy minute number accounting for 68.48% of the total. The average R and LWC (Figure 4c,h) also showed that there were larger R_s and LWC_s than at other times during the three periods. For the three periods, the average values of R and LWC varied from 0.41 to 2.13 $\text{mm} \cdot \text{h}^{-1}$, from 0.04 to 0.09 $\text{g} \cdot \text{m}^{-3}$;

$1.88 \text{ mm} \cdot \text{h}^{-1}$, and $0.15 \text{ g} \cdot \text{m}^{-3}$; from 0.53 to $1.41 \text{ mm} \cdot \text{h}^{-1}$, from 0.04 to $0.17 \text{ g} \cdot \text{m}^{-3}$, respectively. The average N_t and N_w (Figure 4d,f) show the same diurnal variation. Specifically, the average N_t and N_w of the three periods from 02:00 to 09:00 CST, from 12:00 to 13:00 CST, and from 17:00 to 19:00 CST are larger than those at other times. In these three periods, the average values of N_t and N_w were in the ranges of 2.13×10^2 – $5.29 \times 10^2 \text{ m}^{-3}$, 4.57×10^2 – $1.45 \times 10^3 \text{ mm}^{-1} \cdot \text{m}^{-3}$; 4.61×10^2 – $5.31 \times 10^2 \text{ m}^{-3}$, and 1.15×10^3 – $1.86 \times 10^3 \text{ mm}^{-1} \cdot \text{m}^{-3}$; 3.76×10^2 – $5.01 \times 10^2 \text{ m}^{-3}$, 9.33×10^2 – $1.18 \times 10^3 \text{ mm}^{-1} \cdot \text{m}^{-3}$, respectively. The average of D_m (Figure 4e) from 14:00 to 21:00 CST and the average of Z (Figure 4g) from 12:00 to 21:00 CST are generally larger than other time periods. For the two periods, the range of the average values of D_m and Z are 0.87 – 1.28 mm and 16.26 – 23.84 dBZ , respectively. Upon comparing the averages and medians of R , N_t , D_m , and LWC , we found that most of the averages were higher than the medians, implying that the majority of precipitation events had lower values for these quantities than the averages. In addition, the changes in the medians and the averages of these quantities over time are more drastic and evident from 12:00 to 21:00 CST (which is daytime in local time) than other times; correspondingly, Figure 3 shows a lower CBH, lower CTH, and a higher CLN during this period.

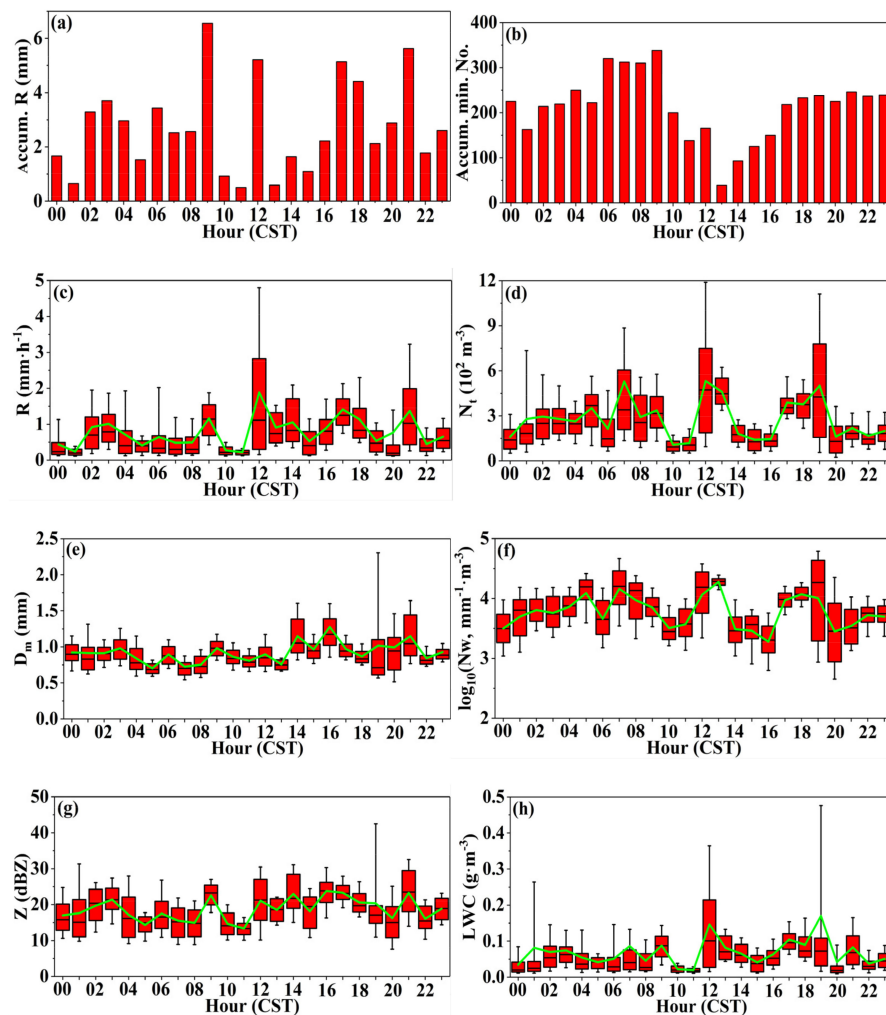


Figure 4. Diurnal variations in (a) accumulated rain amount, (b) accumulated rainy minute number, (c) precipitation intensity (R) ($\text{mm} \cdot \text{h}^{-1}$), (d) number concentration of total raindrops (N_t) (m^{-3}), (e) mass-weighted mean diameter (D_m) (mm), (f) normalized intercept parameter (N_w) ($\text{mm}^{-1} \cdot \text{m}^{-3}$), (g) radar reflectivity (Z) (dBZ), and (h) liquid water content (LWC) ($\text{g} \cdot \text{m}^{-3}$) during the observation period. The green line represents the average, on each box, the central crossbar indicates the median, and the bottom and top edges of the box indicate the 25th and 75th percentiles, respectively. The black whiskers extend to the maximum and minimum of the data points, respectively.

Clouds and precipitation in Xinjiang have local diurnal characteristics. However, it is unclear what the characteristics of the DSD are, whether the $Z - R$ relationships in other areas are applicable to Xinjiang, and what the differences of physical parameters of raindrops between arid Xinjiang and humid regions in China are, etc. Based on these issues, further research is carried out in Sections 3.2–3.6.

3.2. Composite Raindrop Spectra

In this subsection, the DSD characteristics for stratiform and stratocumulus rains are analyzed and compared. According to the classification of rainfall types in Figure 2, we obtained 2753 samples of stratiform rainfalls and 754 samples of stratocumulus rainfalls. Additionally, the process of convective precipitation occurs less frequently, over a shorter time, and changes drastically in the arid area of Xinjiang [52,53,56] resulting in very few valid convective rainfall samples. Therefore, we used the moment method to fit the DSDs of stratiform precipitation and stratocumulus precipitation to the normalized gamma function $N(D) = N_w \cdot f(\mu) \cdot \left(\frac{D}{D_m}\right)^\mu \cdot \exp\left[-(4 + \mu)\frac{D}{D_m}\right]$ that characterizes the DSD distribution. Figure 5 is the composite raindrop spectrum for stratiform and stratocumulus rain and its fit to the normalized gamma distribution model. The average and fitted spectra of stratiform precipitation and stratocumulus precipitation are close, indicating that the DSDs of these two types of precipitation are relatively similar. Furthermore, Table 1 shows that the average values of N_t , $\log_{10}N_w$, W , R , D_m , and Z of stratiform precipitation are 312 m^{-3} , $3.86 \text{ m}^{-3} \cdot \text{mm}^{-1}$, $0.07 \text{ g} \cdot \text{m}^{-3}$, $0.89 \text{ mm} \cdot \text{h}^{-1}$, 0.90 mm , and 19.24 dBZ , respectively. Simultaneously, the values of these physical quantities of stratocumulus precipitation are slightly higher, and the average values of the shape factor μ are 9.74 and 8.76, respectively, which are quite different from the fixed value in the WDM6 and Thompson microphysical parameterization scheme in WRF. Therefore, we focus analysis on the stratiform precipitation, which has more samples, in the following sections.

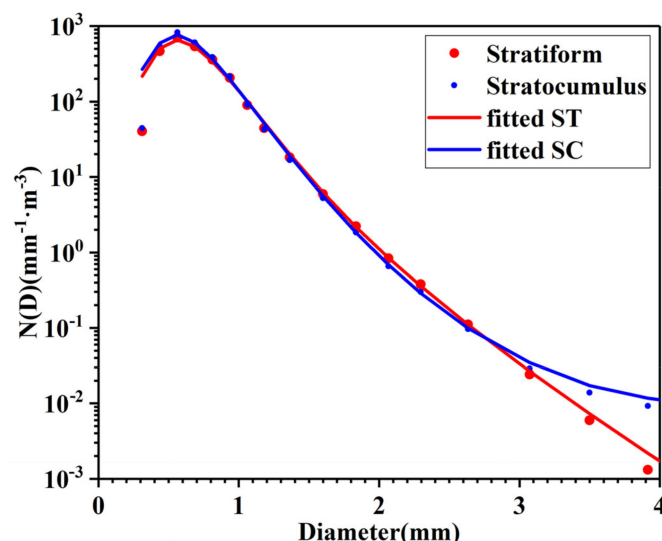


Figure 5. Raindrop size distributions (DSDs) and Gamma distribution fitting curves for stratiform and stratocumulus precipitation.

Table 1. Average values of microphysical parameters for stratiform and stratocumulus precipitation.

Rain Type	$N_t (\text{m}^{-3})$	$\log_{10}N_w (\text{m}^{-3} \cdot \text{mm}^{-1})$	$W (\text{g} \cdot \text{m}^{-3})$	$R (\text{mm} \cdot \text{h}^{-1})$	$D_m (\text{mm})$	$Z (\text{dBZ})$	μ
Stratiform	312	3.86	0.07	0.89	0.90	19.24	9.74
Stratocumulus	351	3.89	0.08	0.90	0.94	20.85	8.76

3.3. $N_t - R$, $D_m - R$, $N_w - R$, and $N_t - N_w$ Relationship

In this subsection, empirical relationships of rainfall physical quantities for stratiform precipitation are proposed. The value of N_t usually increases with the increase in the R . Their relationship was given by Ulbrich et al. [28] as $N_t = \xi R^\eta$. Jin et al. [69] provided the relationship for stratiform rainfall in the area between the Yangtze River and Huaihe River in eastern China as $\log_{10} N_t = 2.14R^{0.14}$. Figure 6a shows the scatterplots of $\log_{10} N_t$ and R and the curve fitted by the least square method for the Xinjiang data. The fitting equation is $\log_{10} N_t = 2.50R^{0.09}$ and has a larger coefficient and a smaller exponent than Jin et al. [69], and the correlation coefficient of the $\log_{10} N_t - R$ relationship is 0.65. Compared to the humid eastern region of China, the arid Xinjiang region needs a greater N_t to produce the same R . Similarly, when N_t is the same, the R in Xinjiang is smaller than in eastern China.

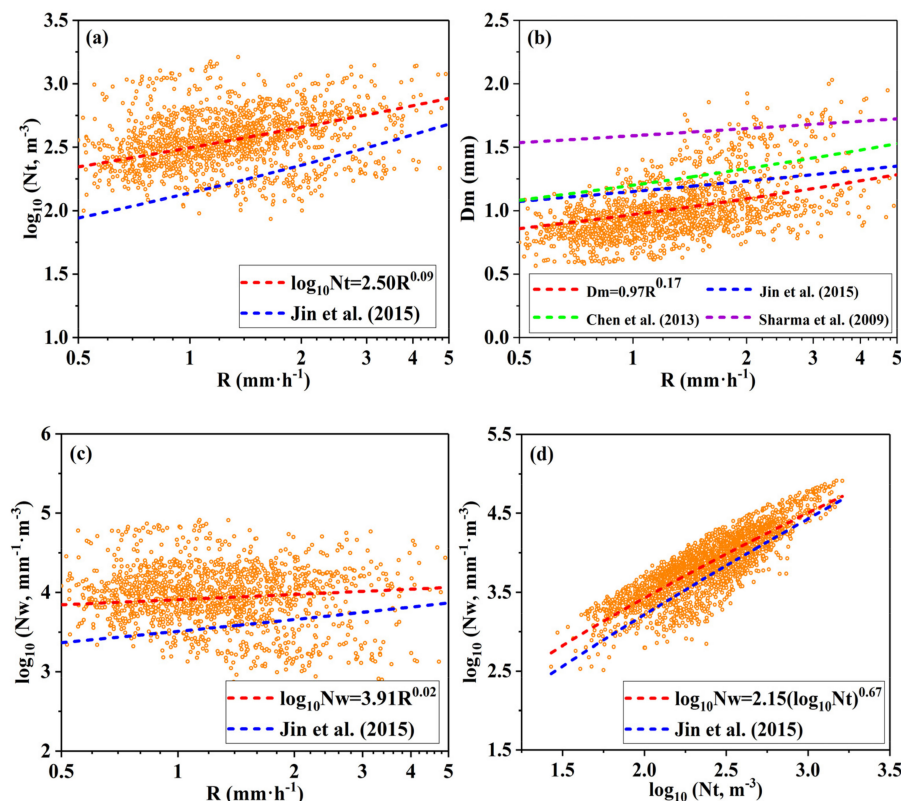


Figure 6. (a) Scatterplots of the $\log_{10} N_t - R$ relationship, (b) scatterplots of the $D_m - R$ relationship, (c) scatterplots of the $\log_{10} N_w - R$ relationship, and (d) scatterplots of the $\log_{10} N_w - \log_{10} N_t$ relationship. The red dashed curve is the fitted curve for stratiform precipitation in Xinjiang.

Sharma et al. [41] studied the relationship between D_m and R based on the raindrop spectrum data in the Gadanki region of India and obtained the $D_m - R$ relationship of stratiform precipitation as $D_m = 1.59R^{0.05}$. Chen et al. [30] fit the $D_m - R$ relationship of stratiform precipitation in the Nanjing area of China as $D_m = 1.20R^{0.15}$. The $D_m - R$ relationship of stratiform precipitation in the area between the Yangtze River and Huaihe River in eastern China is fitted as $D_m = 1.15R^{0.10}$. In this study, the $D_m - R$ relationship in Xinjiang is fitted as $D_m = 0.97R^{0.17}$ (Figure 6b), and its coefficient is smaller, and the index is larger than the values of the other three regions. Simultaneously, for the same R , the Xinjiang area has a smaller D_m than the other three regions, which indicates that the raindrop size is smaller in the arid Xinjiang area.

Figure 6c shows the scatterplots and fitted curve of the $\log_{10} N_w - R$ relationship. Jin et al. [69] gave the relationship for the stratiform rainfall in the area between the Yangtze River and the Huaihe River in eastern China as $\log_{10} N_w = 3.51R^{0.06}$. In Xinjiang, the fit relationship is $\log_{10} N_w = 3.91R^{0.02}$. With the same R , N_w in the arid Xinjiang is larger than N_w in the humid area between the Yangtze River

and the Huaihe River, which is consistent with the $\log_{10} N_w - R$ relationship in Figure 6a. However, Testud et al. [59] highlighted that there is no evident relationship between $\log_{10} N_w$ and R , which was also confirmed by the results of Jin et al. [69]. In this study, their correlation coefficient is 0.22, which also proves that $\log_{10} N_w$ and R have no evident correlation.

Figure 6d shows the scatterplots and fitted curve of the $\log_{10} N_w - \log_{10} N_t$ relationship. The $\log_{10} N_w - \log_{10} N_t$ relationship for the stratiform rainfall in the area between the Yangtze River and the Huaihe River in eastern China was provided by Jin et al. [69] as $\log_{10} N_w = 1.86(\log_{10} N_t)^{0.79}$. In arid Xinjiang, the formula for the fitted curve is $\log_{10} N_w = 2.15(\log_{10} N_t)^{0.67}$ with larger coefficients and smaller exponents. Simultaneously, the correlation coefficient of $\log_{10} N_w$ and $\log_{10} N_t$ is as high as 0.85, indicating that N_w , as an independent parameter, can effectively reflect the concentration of raindrops.

3.4. Z – R Relationship

Empirical relationship of $Z - R$ for stratiform precipitation in Xinjiang is proposed based on the data of the disdrometer and Formulas (2) and (4) in this subsection. The empirical formula $Z = AR^b$ is the basis for the QPE by radar. However, Rosenfeld et al. [63] pointed out that topography, atmospheric conditions, precipitation types, and other factors lead to differences in the distribution of raindrops, which in turn leads to changes in the $Z - R$ relationship. For this reason, many previous researchers have given different $Z - R$ relationships for stratiform rainfall in other regions [39,41,69–73]. From the Tropical Ocean Global Atmosphere Coupled Ocean–Atmosphere Experiment, Tokay et al. [26] provided the $Z - R$ relationship for stratiform rainfall as $Z = 367R^{1.30}$. Maki et al. [39] used the disdrometer data measured in Darwin, Australia, to give the relationship for stratiform rainfall as $Z = 532R^{1.28}$. From the African Monsoon Multidisciplinary Analysis (AMMA) field campaign, $Z = 562R^{1.44}$ was given by Moumouni et al. [72]. These are the results provided by the researchers using the raindrop spectrum data of low-latitude tropical areas. For the monsoon region of eastern China located in the subtropical region, Jin et al. [69] and Huang et al. [73] used the raindrop spectrum data of Chuzhou and Nanjing, China, to give the $Z - R$ relationship for stratiform rainfall as $Z = 301R^{1.21}$ and $Z = 200R^{1.48}$, respectively. The value of the coefficient and the index in the $Z - R$ relationship change, and the locality is evident. For the arid Xinjiang, the fitted $Z - R$ relationship is $Z = 249R^{1.20}$ using the least squares method with the smallest exponent and smaller coefficient than those given in the above study (Figure 7). The correlation coefficient of the $Z - R$ relationship is 0.78, and the RMSE of R measured by the disdrometer and R derived from the $Z - R$ relationship is $0.99 \text{ mm} \cdot \text{h}^{-1}$.

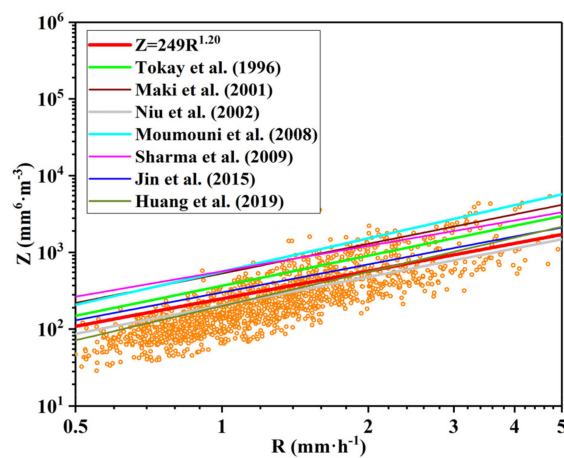


Figure 7. Scatterplots of Z versus R and the fitted relationship for stratiform rainfall. The red curve is the fitted curve for stratiform precipitation in Xinjiang, and the orange circles represent the scattered points of the $Z-R$ relationship obtained from the disdrometer data.

3.5. $Z/D_m - R$ Relationship

In this subsection, the $Z/D_m - R$ relationship is established for stratiform rainfall in Xinjiang. Testud et al. [59] highlighted that an empirical relationship involving a single measurement parameter Z may not provide desired rain retrieval accuracy. Sharma et al. [41] considered another parameter D_m , using Z/D_m and R to establish a new empirical relationship $Z/D_m = 342R^{1.07}$ for stratiform rainfall, and significant improvement is observed in rain retrieval by using the $Z/D_m - R$ relationship relative to the conventional $Z - R$ relation. In this study, we used the scatterplots of Z/D_m and R to establish a fitting curve as $Z/D_m = 214R^{1.12}$ (Figure 8), which has a smaller coefficient and a larger exponent than the relation given by Testud et al. [59]. More importantly, the correlation coefficient of $Z/D_m - R$ of 0.88 is larger than that of $Z - R$ of 0.78 (Table 2). Simultaneously, the root mean square error is reduced from $0.99 \text{ mm} \cdot \text{h}^{-1}$ of R measured by the disdrometer and R derived from the $Z - R$ relationship to $0.92 \text{ mm} \cdot \text{h}^{-1}$ of R measured by the disdrometer and R derived from the $Z/D_m - R$ relationship. There is an improvement in rain retrieval by using the $Z/D_m - R$ relation compared to the conventional $Z - R$ relation. Table 2 shows the CCs of all empirical relationships established in this study for stratiform rainfall in Xinjiang. Notably, the order of the correlation coefficient is $Z/D_m - R > \log_{10} N_w - \log_{10} N_t > Z - R > \log_{10} N_t - R > D_m - R > \log_{10} N_w - R$.

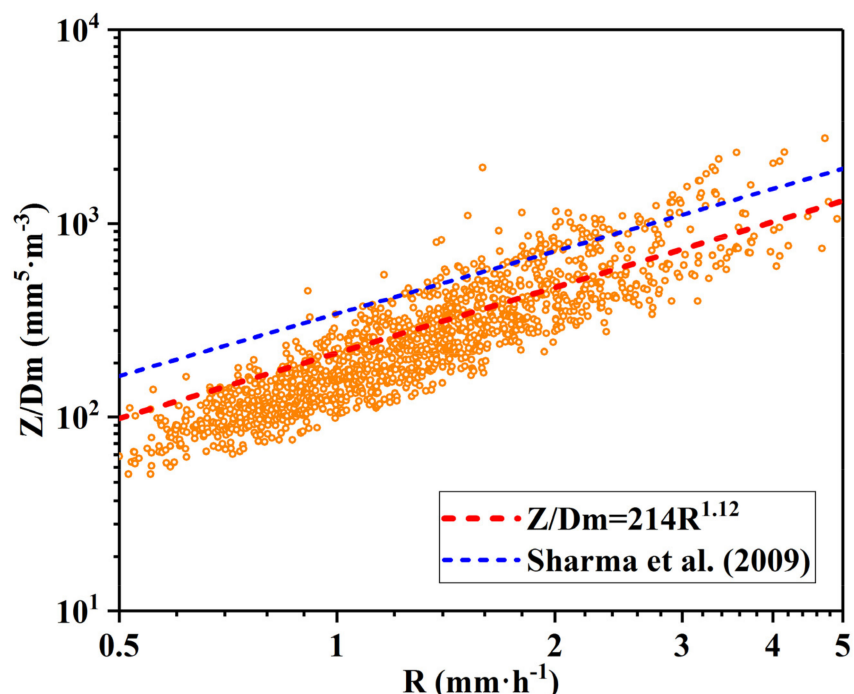


Figure 8. Scatterplots of Z/D_m versus R and the fitted relationship for stratiform rainfall. The red dashed curve is the fitted curve for stratiform precipitation in Xinjiang.

Table 2. Correlation coefficients for different empirical relations for the 2753 samples of stratiform rainfalls.

Relation	$\log_{10} N_t - R$	$D_m - R$	$\log_{10} N_w - R$	$\log_{10} N_w - \log_{10} N_t$	$Z - R$	$Z/D_m - R$
Correlation coefficient	0.65	0.62	0.22	0.85	0.78	0.88

3.6. Case Study

The rainfall estimation relationships derived above are based on the statistical relationship. Whether they are applicable in a case and what the specific performances are in a case need to be discussed further. In this subsection, we compared the R estimated from the $Z - R$ relationship and the $Z/D_m - R$ relationship through a case study of data from 20 to 21 May 2020. Figure 9a shows

that the curve of R estimated from the $Z/D_m - R$ relationship is closer to the curve of R measured by the disdrometer than the curve of the R estimated from the $Z - R$ relationship. Their correlation coefficients are 0.93 and 0.88, and the root mean square errors are $1.11 \text{ mm} \cdot \text{h}^{-1}$ and $1.29 \text{ mm} \cdot \text{h}^{-1}$, respectively. The R obtained from the $Z/D_m - R$ relationship can better estimate R measured by the disdrometer. Figure 9b shows the variation of several characteristic physical quantities over time in this case. Among them, the change trends of Z , D_m , and LWC are relatively consistent, and the change of N_t has its own characteristics. The second precipitation event that occurred after 21:00 CST on 20 May has two different precipitation stages with different characteristics of characteristic physical quantities. Comparing the values of characteristic physical quantities at 22:30 CST on 20 May and 02:36 CST on 21 May, we can see that the N_t was only 249.22 m^{-3} at 22:30 CST on 20 May, but Z , D_m , and LWC were 35.60 dBZ , 1.78 mm , and $0.21 \text{ g} \cdot \text{m}^{-3}$, respectively. The N_t was 431.99 m^{-3} at 02:36 CST on 21 May, but Z , D_m , and LWC were only 20.04 dBZ , 0.82 mm , and $0.08 \text{ g} \cdot \text{m}^{-3}$, respectively. It shows that, although the total number of raindrops is small, the number of big raindrops is large at 22:30 CST on 20 May, and their contribution to Z , D_m , and LWC is greater.

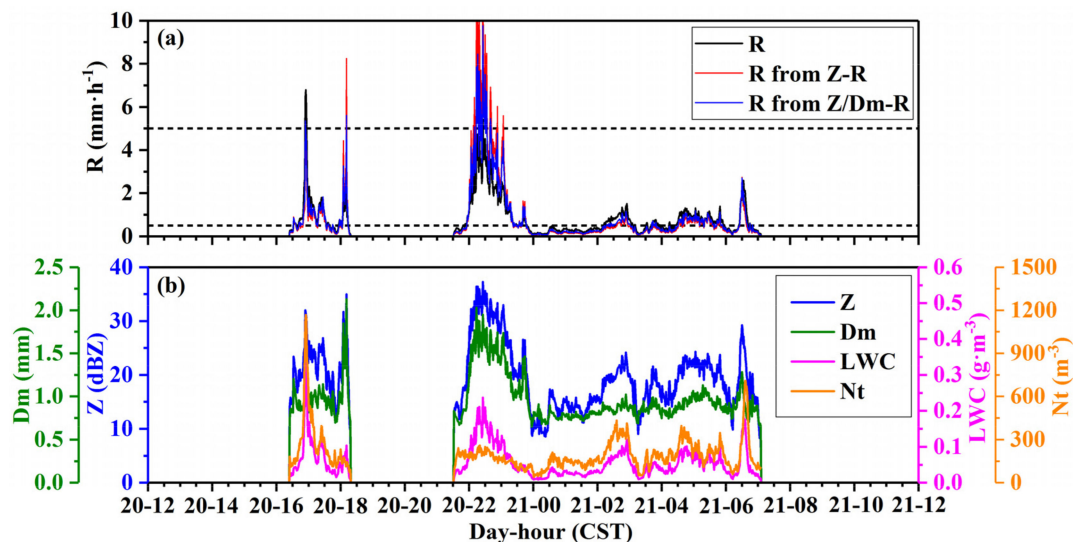


Figure 9. (a) Temporal variation of estimated rain intensity ($\text{mm} \cdot \text{h}^{-1}$) by using $Z - R$, $Z/D_m - R$ relations and measured by the disdrometer and (b) Z (dBZ), D_m (mm), LWC ($\text{g} \cdot \text{m}^{-3}$), and N_t (m^{-3}) on 20–21 May 2020.

In order to show that the data from the MMCR and the data from the disdrometer are consistent and reliable and these physical quantities are meaningful, we also draw the relevant physical quantity profile from the MMCR in this case. Figure 10 shows the time–height profile of the radar reflectivity factor, Doppler velocity (positive value upwards), and velocity spectrum width of the case study data observed by the MMCR. The artifacts between 4 and 6 km are caused by processing issues of MMCR. Specifically, when MMCR detects precipitation, it must ensure the detection range and the detection sensitivity at the same time. Therefore, different detection modes are adopted, and discontinuous artifacts inevitably appear in the process of using wide pulse and narrow pulse detection, which is the so-called pulse complementary technology. Similarly, the second precipitation event can be divided into two stages. The first stage is before 01:00 CST on 21 May. The reflectance factor, Doppler velocity, and velocity spectrum width change is observable. The value of the strongest reflectivity factor is below 2 km and reaches 40 dBZ (Figure 10a), which is similar to that observed by the disdrometer in Figure 9b. Correspondingly, the maximum downward Doppler velocity (Figure 10b) and velocity spectrum width (Figure 10c) reach $8 \text{ m} \cdot \text{s}^{-1}$ and $3 \text{ m} \cdot \text{s}^{-1}$ at this stage, respectively. The second stage is after 01:00 CST on 21 May, the reflectance factor, Doppler velocity, and velocity spectrum width change relatively smoothly with time, which is consistent with the trend of R , N_t , Z , D_m , and LWC in Figure 9.

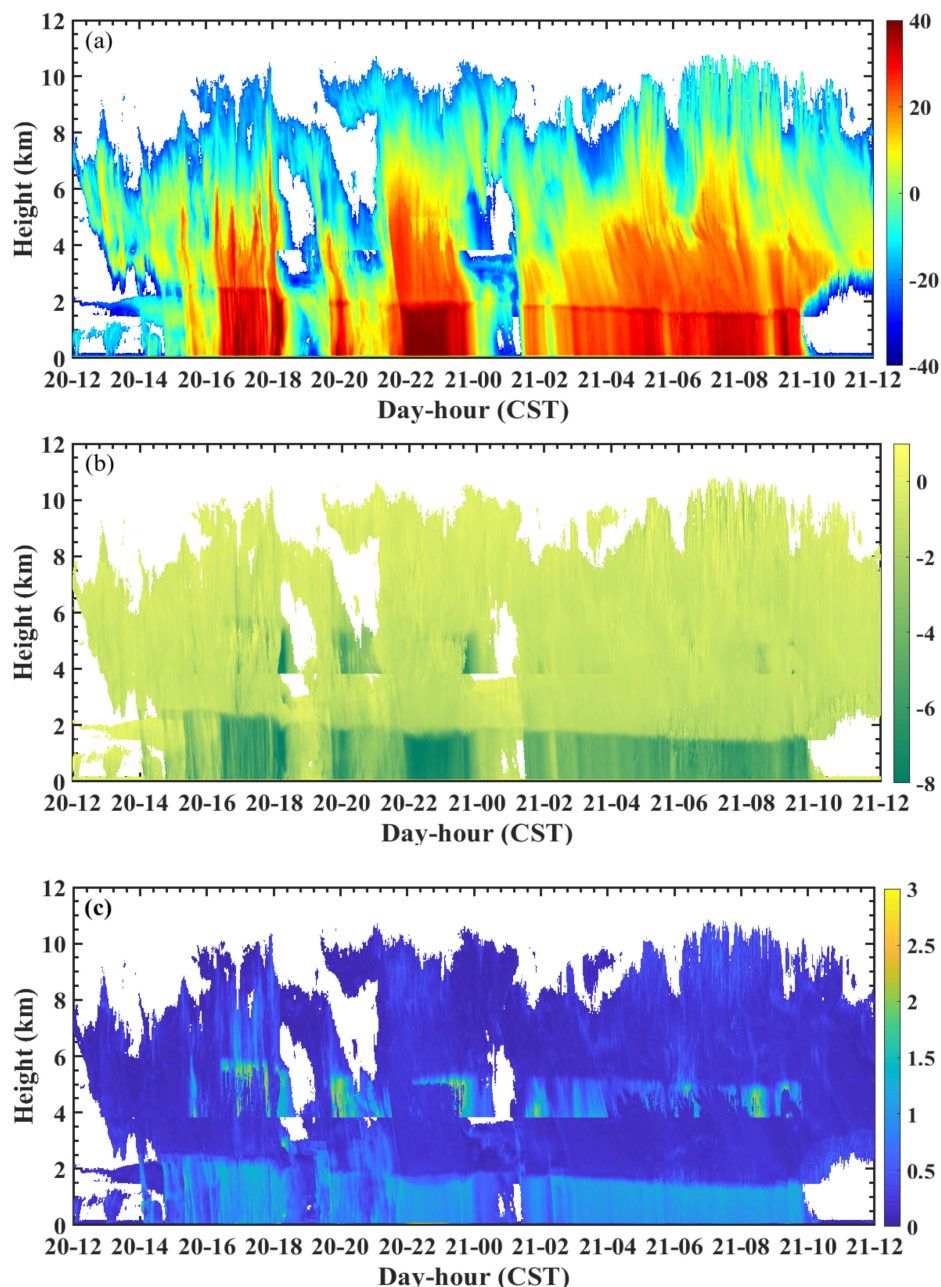


Figure 10. Time–height profile of the (a) radar reflectivity factor (dBZ), (b) Doppler velocity ($\text{m} \cdot \text{s}^{-1}$), and (c) velocity spectrum width ($\text{m} \cdot \text{s}^{-1}$).

4. Discussion

The characteristics of clouds and precipitation are of importance for understanding the formation process for clouds and rain [5–7,22–25,74]. However, these characteristics differ depending on location because of the differences in climate, atmospheric conditions, and topography [26–28]. Previous studies have mostly focused on clouds and precipitation in the monsoon region, and those research conclusions are of importance for the improvement of microphysical parameterization of the model and quantitative precipitation estimation by radar and can further reveal the feedback effects of clouds and precipitation in climate change. However, there are scarce studies on clouds and precipitation in arid regions. We carried out our study in an arid region to reveal any characteristics of diurnal variation in clouds and precipitation, with the results showing that there is a big difference in diurnal behavior from the monsoon regions in eastern China. For example, in southern China during the summertime,

many clouds are distributed below 3 km and are most prominent at sunrise, noon, and sunset [20]. In South China during the pre-flood season, the warm clouds are mainly distributed at low altitude, below 2.5 km [21]. Our research found that the cloud height is higher, and the daily variations are more evident in the arid region of Xinjiang. The diurnal variations of clouds and precipitation are closely related to incoming solar radiation values [20,21], with the higher temperature during the daytime (Figure 11a) conducive to the enhancement of atmospheric instability. In addition, the trumpet-shaped topography that opens to the west of the observation site (Figure 1) has an important influence on airflow through the Tianshan mountains. The mountain–valley wind circulation (Figure 11b) formed by a westerly wind from the valley to the mountains during the daytime and an easterly wind from the mountains to the valley during the nighttime may also play an important role. In fact, the diurnal variation of clouds and the diurnal variation of rainfall need to be discussed separately because their diurnal variation mechanisms are different. The diurnal variation of clouds is mainly driven by wind and temperature, that is, dynamic and thermal effects (Figure 12). It should be noted that the clouds we studied do not distinguish between precipitation days and non-precipitation days, and the clouds on non-precipitation days account for the vast majority of our statistics, therefore, the diurnal variation of clouds in the study can be regarded as the diurnal variation of the cloud on non-rainfall days. Under the influence of westerly winds during the daytime, the low-level airflow has a climbing and ascending motion, and the heating effect of solar radiation increases the instability of the low-level atmosphere, thereby making the exchange of matter and energy in the boundary layer become active. Under such dynamic and thermal conditions, clouds tend to form at lower altitudes during the daytime. On the contrary, the cold air from the top of the mountain at nighttime moves downward and westward, and the sinking movement combined with the lower temperature makes the lower atmosphere stable, which is not conducive to the formation of clouds in the lower atmosphere. At the same time, some of the higher clouds near the top of the mountain moved to the sky above Xinyuan under the influence of easterly air currents. The above physical processes cause the cloud base and cloud top to be higher at night than during the day. Of course, are the above-mentioned diurnal variations of precipitation related to the diurnal variations of the eastward system? Does the system causing the rain reach the study area at the same time every day? To answer the above questions, all rainfall events are listed from this study in Table 3. Simultaneously, to see the diurnal variations of each rainfall event more clearly, the start, duration and end times of each rainfall event are shown in Figure 13. From Table 3 and Figure 13, we can see that the time of occurrence of rainfall events has a strong impact on the diurnal variations of rainfall. The diurnal variations of rainfall are mainly determined by the time period of the specific rainfall process, and temperature also plays a certain role. For example, the number of rainfall events starting and sustaining at 16:00–18:00 is significantly more than the number of rain events at 13:00–15:00, corresponding to the number of rainfall events, the former has significantly more accumulated rain amount and accumulated rainy minute number than the latter. Therefore, the appearance time of the eastward movement system that causes rainfall every day in each rainfall event has an important impact on the diurnal variations of clouds and rainfall. Correspondingly, the satellite imagery from Fengyun 2-G satellite (FY-2G) at the beginning of each rainfall event is also displayed (Figure 14). The time for the rain cloud system to move to the rainfall area in each rainfall event is not evenly distributed in 24 h. Some times are easily controlled by rain clouds, while other times are rarely affected by rain clouds, and there are differences in each rain cloud, and the higher temperature during the day strengthens the diurnal variation of rainfall, that is, the rainfall during the daytime is more intense than at nighttime (for example, it can be clearly seen from Figure 4c,e). So the above-mentioned factors are the key and main factors that affect the characteristics of the diurnal variations of clouds and precipitation, the diurnal variation of clouds is mainly driven by wind and temperature closely related to the topography of the study area, and the daily variation of rainfall is mainly determined by the time period of the specific rainfall process, and temperature also plays a certain role.

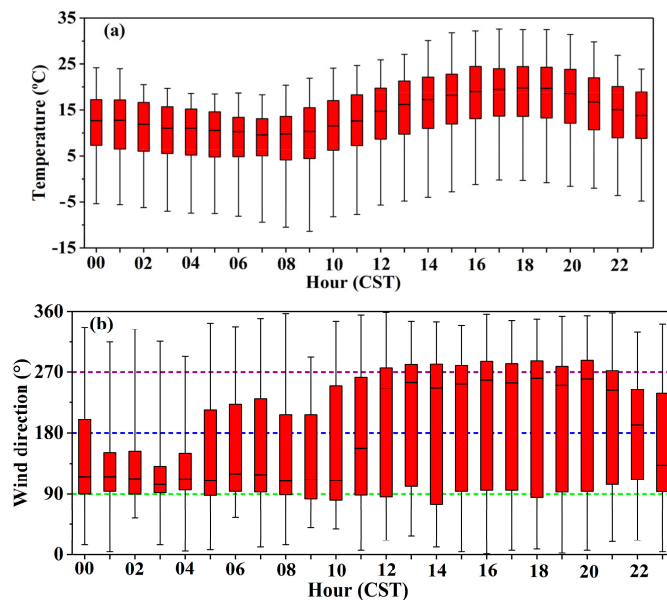


Figure 11. Diurnal variations in (a) temperature at 2 m ($^{\circ}$ C), and (b) wind direction at 10 m ($^{\circ}$) during the observation period at Xinyuan Meteorological Station. On each box, the central crossbar indicates the median, and the bottom and top edges of the box indicate the 25th and 75th percentiles, respectively. The black whiskers extend to the maximum and minimum of the data points, respectively. The green dashed, blue dashed and purple dashed lines are the positions of east wind, south wind and west wind, respectively.

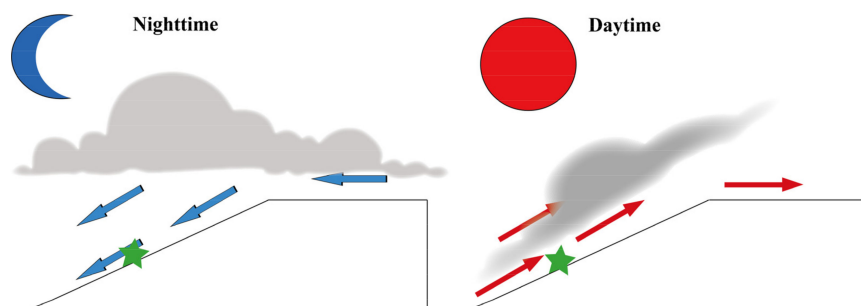


Figure 12. Schematic diagram of the diurnal variation of clouds (the green five-pointed star represents the position of the new source).

Table 3. The start and end time, accumulated rain amount and average rainfall intensity of each precipitation event.

Number of Rain Event	Start and End Time (Month/Day/Hour:Minute)	Accumulated Rain Amount (mm)	Average Rainfall Intensity ($\text{mm} \cdot \text{h}^{-1}$)
1	3/6/11:55–3/6/12:52	0.80	0.83
2	3/6/16:48–3/6/18:46	0.45	0.23
3	3/20/05:40–3/20/16:19	7.29	1.07
4	3/22/15:46–3/22/19:09	1.53	0.45
5	3/24/02:02–3/24/02:35	0.22	0.39
6	3/29/03:51–3/29/08:42	2.70	0.89
7	4/9/18:41–4/9/19:43	0.58	0.56
8	4/14/08:45–4/14/09:49	0.87	0.80
9	4/15/11:13–4/15/12:30	0.36	0.28
10	4/15/18:03–4/16/05:06	8.72	0.97
11	4/18/02:19–4/18/09:10	0.19	0.21
12	4/30/18:23–4/30/23:57	8.16	1.46
13	5/3/23:45–5/4/10:52	12.12	1.15
14	5/15/08:32–5/15/10:27	1.15	0.60
15	5/20/16:25–5/20/18:18	2.00	1.05
16	5/20/21:32–5/21/00:00	3.80	1.53
17	5/21/03:01–5/21/09:58	3.35	0.55

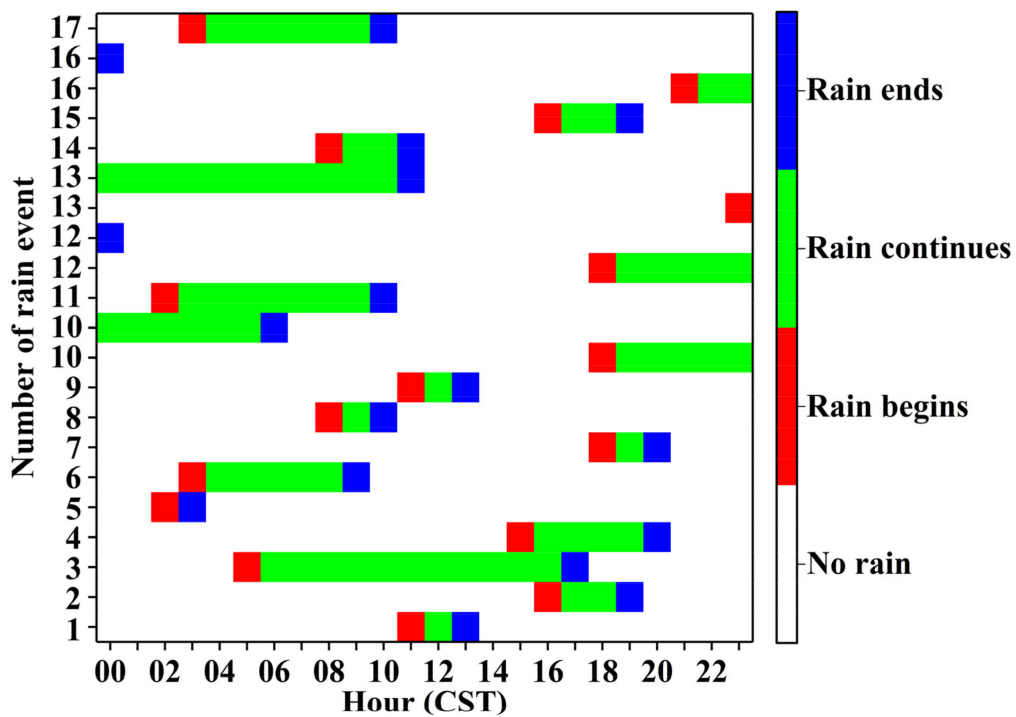


Figure 13. The start, duration and end time of each rain event.

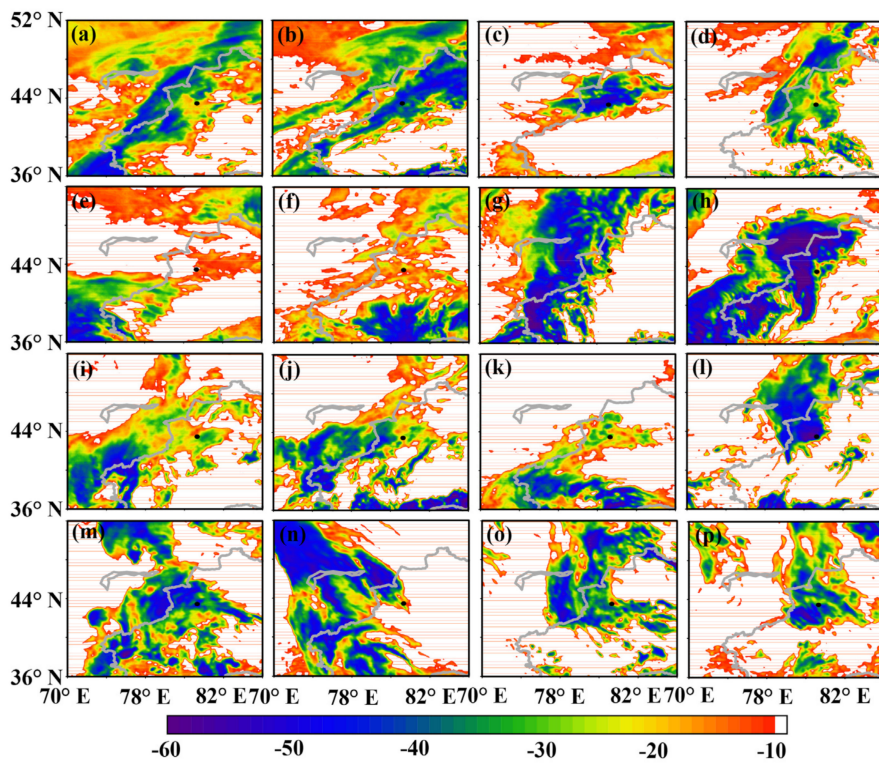


Figure 14. The TBB (black-body temperature) from FY-2G (Fengyun 2-G satellite) at the beginning of each rainfall event, rainfall event 1 to rainfall event 17 are (a–p), respectively (except rainfall event 16, because rainfall event 16 and rainfall event 15 are affected by the same system).

Further analysis of the raindrop spectrum distribution, microphysical parameters, and $Z - R$ relationship in arid areas showed that it is significantly different from other regions. For example, the average values of N_t for the stratiform precipitation in Zhuhai in the monsoon region of China [67]

and Xinjiang in the arid region of China are 111 m^{-3} and 312 m^{-3} , respectively, and the average values of LWC , R , and D_m are also significantly different. The average values of the three physical parameters of these two regions are $0.52 \text{ g} \cdot \text{m}^{-3}$, $1.66 \text{ mm} \cdot \text{h}^{-1}$, 1.53 mm and $0.07 \text{ g} \cdot \text{m}^{-3}$, $0.89 \text{ mm} \cdot \text{h}^{-1}$, 0.90 mm , respectively. The rain in arid Xinjiang had a relatively higher concentration of raindrops and a smaller average raindrop diameter than the rain in humid regions. Based on the $Z - R$ relationship, the $Z/D_m - R$ relationship has been developed, which has a better estimation effect on rain intensity. These results are useful for revealing the microphysical characteristics of clouds and precipitation, thereby improving the QPE for this area and improving the microphysical parameterization scheme to update the precipitation forecast in this area. Since full comparison with the results of other arid regions, these findings may be applicable to other arid regions worldwide with similar atmospheric conditions and topographical conditions as Xinjiang. However, our research results are limited because we only used data from March 1 to May 31, 2020. In the future, this preliminary study should be expanded with more observational data, taking into account seasonal and yearly variability [43].

5. Conclusions

In this study, the observation data of the Ka-band MMCR and disdrometer from March 1 to May 31, 2020, in Xinjiang, a typical arid region of China, were used to reveal the diurnal variation of the characteristics of clouds and precipitation, DSD, and physical parameters of raindrops. The main conclusions are as follows.

1. Approximately half of CBHs, CTHs, and CTNs varied from 60 to 2075 m, 4350 to 7715 m, and 1770 to 5181 m, respectively. Diurnal variation shows a decreasing trend of CBHs from 05:00 to 19:00 CST and a rising trend of CBHs from 20:00 to 04:00 CST. The CTHs show the rising trend from 03:00 to 05:00 CST, 12:00 to 14:00 CST, and 20:00 to 01:00 CST, respectively, and 75% of the total samples of CTHs were above 5000 m from 00:00 to 09:00 CST. There was also a large number of CTHs below 3 km from 10:00 to 23:00 CST. Approximately 50% of the CTNs show the characteristics of the diurnal variation similar to the CTHs. The CTNs less than 2 km and the frequency distribution of CLNs are significantly increased from 10:00 to 23:00 CST. There are three obvious precipitation periods during the day, namely, 02:00–09:00 CST, 12:00 CST, and 17:00–21:00 CST, and the three periods produced 79.18% of the entire accumulated rain amount and 68.48% of the entire accumulated rainy minute numbers, and there were larger R_s and $LWCs$ during the three periods. Other physical parameters also showed diurnal variation. In general, the changes were more evident during the period 12:00–21:00 CST. The diurnal variation of clouds is mainly driven by wind and temperature closely related to the topography of the study area, and the daily variation of rainfall is mainly determined by the time period of the specific rainfall process, and temperature also plays a certain role.
2. The DSD is in good agreement with a normalized gamma distribution. The average value of microphysical parameters for the N_t , $\log_{10}N_w$, W , R , D_m , and Z of stratiform precipitation are 312 m^{-3} , $3.86 \text{ m}^{-3} \cdot \text{mm}^{-1}$, $0.07 \text{ g} \cdot \text{m}^{-3}$, $0.89 \text{ mm} \cdot \text{h}^{-1}$, 0.90 mm , and 19.24 dBZ , respectively, and the values of these physical quantities for stratocumulus precipitation are slightly larger, and the shape factor μ are 9.74 and 8.76, respectively, which are quite different from the fixed value in the microphysical parameterization scheme in WRF. The rain in arid Xinjiang had a relatively higher concentration of raindrops and a smaller average raindrop diameter than the rain in humid regions. The fitting equation of $N_t - R$, $D_m - R$, $N_w - R$, and $N_t - N_w$ relationship for stratiform precipitation suitable for Xinjiang are $\log_{10}N_t = 2.50R^{0.09}$, $D_m = 0.97R^{0.17}$, $\log_{10}N_w = 3.91R^{0.02}$, and $\log_{10}N_w = 2.15(\log_{10}N_t)^{0.67}$, respectively.
3. For the arid Xinjiang, the $Z - R$ relationship of stratiform precipitation is $Z = 249R^{1.20}$. The correlation coefficient of $Z - R$ relationship is 0.78, and the RMSE of R measured by the disdrometer and R derived from the $Z - R$ relationship is $0.99 \text{ mm} \cdot \text{h}^{-1}$. Z/D_m and R are used to establish a new empirical relationship $Z/D_m = 214R^{1.12}$ for stratiform rainfall. The correlation coefficient of the $Z/D_m - R$ relationship is 0.88, and the root mean square error

of the R measured by the disdrometer and the R estimated from the $Z/D_m - R$ relationship is $0.92 \text{ mm} \cdot \text{h}^{-1}$. Improvement is obtained in rain retrieval by using the $Z/D_m - R$ relation relative to the conventional $Z - R$ relation. The case study of data from 20 to 21 May 2020, also verified this conclusion.

In summary, the diurnal variation of clouds and precipitation and the characteristics of raindrop spectra have been obtained for a specified period in the typically arid region of Xinjiang and have been shown to be fundamentally different than those of humid regions. Additionally, the $Z - R$ relationship and $Z/D_m - R$ relationship suitable for Xinjiang have been established, which are helpful to understand the formation process of clouds and precipitation in an arid area. They also play a role in the improvement of the microphysical parameters for the model and the improvement of the QPE, enabling meteorological departments to make better use of cloud water resources and improve rainfall forecasting capabilities in arid areas. However, as aforementioned, the observational data for this study are limited to a three-month period, and it is necessary to use longer-term observational data for research on different seasons and different rainfall types in the future.

Author Contributions: Conceptualization, Y.Z.; data curation, Y.Z. and L.Y.; formal analysis, Y.Z.; funding acquisition, L.Y. and Y.Z.; methodology, Y.Z., Z.Z. and J.Z.; project administration, J.Z., F.L. and Z.Z.; resources, J.L. and Z.T.; supervision, L.Y., Y.J. and Z.T.; writing—original draft, Y.Z.; writing—review and editing, Y.Z. All authors have read and agreed to the published version of the manuscript.

Funding: This research was funded by the National Key Research and Development Program of China (Grant Nos. 2018YFC1507102, 2018YFC1507104) and Basic Business Expenses (Grant No. IDM2019001).

Acknowledgments: The authors would like to thank the Institute of Desert Meteorology, China Meteorological Administration, Urumqi, for providing the data of Cloud Radar and Disdrometer. Thanks also go to the reviewers for thorough comments that really helped to improve the manuscript.

Conflicts of Interest: The authors declare no conflict of interest.

References

1. Stephens, G.L.; Tsay, S.; Stackhouse, P.W.; Flatau, P.J. The Relevance of the Microphysical and Radiative Properties of Cirrus Clouds to Climate and Climatic Feedback. *J. Atmos. Sci.* **1990**, *47*, 1742–1753. [[CrossRef](#)]
2. Heymsfield, A.J.; Platt, C.M.R. A Parameterization of the Particle Size Spectrum of Ice Clouds in Terms of the Ambient Temperature and the Ice Water Content. *J. Atmos. Sci.* **1984**, *41*, 846–855. [[CrossRef](#)]
3. Ding, S.G.; Shi, G.Y.; Zhao, C.S. Analysis of variation and effect on the climate of cloud amount in China over past 20 years using ISCCP D2. *Chin. Sci. Bull.* **2004**, *49*, 1105–1111. (In Chinese)
4. Zhao, C.S.; Tie, X.; Brasseur, G. Aircraft measurements of cloud droplet spectral dispersion and implications for indirect aerosol radiative forcing. *Geophys. Res. Lett.* **2006**, *33*. [[CrossRef](#)]
5. Ackerman, T.P.; Stokes, G.M. The Atmospheric Radiation Measurement Program. *Phys. Today* **2003**, *56*, 38–45. [[CrossRef](#)]
6. Harrison, E.F.; Minnis, P.; Barkstrom, B.R.; Ramanathan, V.; Cess, R.D.; Gibson, G.G. Seasonal variation of cloud radiative forcing derived from the earth radiation budget experiment. *J. Geophys. Res.* **1990**, *95*, 18687–18703. [[CrossRef](#)]
7. Schiffer, R.A.; Rossow, W.B. The International Satellite Cloud Climatology Project (ISCCP)—The first project of the World Climate Research Programme. *Bull. Am. Meteorol. Soc.* **1983**, *64*. [[CrossRef](#)]
8. Reddy, N.N.; Ratnam, M.V.; Basha, G.; Ravikiran, V. Cloud Vertical Structure over A Tropical Station Obtained Using Long-term High-resolution Radiosonde Measurements. *Atmos. Chem. Phys.* **2018**, *18*, 11709–11727. [[CrossRef](#)]
9. Chen, S.S.; Kerns, B.W.; Guy, N.; Jorgensen, D.P.; Savarin, A. Aircraft Observations of Dry Air, the ITCZ, Convective Cloud Systems, and Cold Pools in MJO during DYNAMO. *Bull. Am. Meteorol. Soc.* **2016**, *97*, 405–423. [[CrossRef](#)]
10. Yang, Y.J.; Lu, D.R.; Fu, Y.F.; Chen, F.J.; Wang, Y. Spectral Characteristics of Tropical Anvils Obtained by Combining TRMM Precipitation Radar with Visible and Infrared Scanner Data. *Pure Appl. Geophys.* **2015**, *172*, 1717–1733. [[CrossRef](#)]

11. Parish, T.R.; Rahn, D.A.; Leon, D. Aircraft Observations of a Coastally Trapped Wind Reversal off the California Coast. *Mon. Weather Rev.* **2008**, *136*, 644–662. [[CrossRef](#)]
12. Parish, T.R.; Leon, D. Measurement of Cloud Perturbation Pressures Using an Instrumented Aircraft. *J. Atmos. Ocean. Tech.* **2013**, *30*, 215–229. [[CrossRef](#)]
13. Field, P.R.; Furtado, K. How Biased Is Aircraft Cloud Sampling? *J. Atmos. Ocean. Tech.* **2016**, *33*, 185–189. [[CrossRef](#)]
14. Dong, X.; Minnis, P.; Xi, B. A climatology of midlatitude continental clouds from ARM SGP site: Part I. Low-level cloud macrophysical, microphysical and radiative properties. *J. Clim.* **2005**, *18*, 1391–1410. [[CrossRef](#)]
15. Xi, B.; Dong, X.; Minnis, P. A 10 year climatology of cloud cover and vertical distribution from both surface and GOES observations over DOE ARM SGP site. *J. Geophys. Res.* **2009**, *115*, D12. [[CrossRef](#)]
16. Hou, A.Y.; Skofronick-Jackson, G.; Stocker, E.F. The Global Precipitation Measurement (GPM) Mission: Overview and U.S. Science Status. *Bull. Am. Meteorol. Soc.* **2014**, *95*, 701–722. [[CrossRef](#)]
17. Kollas, P.; Clothiaux, E.E.; Miller, M.M. Millimeter-wavelength radars: New frontier in atmospheric cloud and precipitation research. *Bull. Am. Meteorol. Soc.* **2007**, *88*, 1608–1624. [[CrossRef](#)]
18. Moran, K.P.; Martner, B.E.; Post, M.J.; Kropfli, R.A.; Widener, K.B. An Unattended Cloud-Proiling Radar for Use in Climate Research. *Bull. Amer. Meteorol. Soc.* **1998**, *79*, 443–455. [[CrossRef](#)]
19. Kollas, P.; Jasmine, R.; Edward, L.; Wanda, S. Cloud radar Doppler spectra in drizzling stratiform clouds: 1. Forward modeling and remote sensing applications. *J. Geophys. Res.* **2011**, *116*. [[CrossRef](#)]
20. Liu, L.; Ruan, Z.; Zheng, J.; Gao, W. Comparing and Merging Observation Data from Ka-band Cloud Radar, C-band Frequency-modulated Continuous Wave Radar and Ceilometer Systems. *Remote Sens.* **2017**, *9*, 1282. [[CrossRef](#)]
21. Zheng, J.; Liu, L.; Chen, H.; Gou, Y.; Che, Y.; Xu, H.; Li, Q. Characteristics of Warm Clouds and Precipitation in South China during the Pre-Flood Season Using Datasets from a Cloud Radar, a Ceilometer, and a Disdrometer. *Remote Sens.* **2019**, *11*, 3045. [[CrossRef](#)]
22. Marshall, J.S.; Palmer, W.M.K. The Distribution of Raindrops with Size. *J. Atmos. Sci.* **1948**, *5*, 165–166. [[CrossRef](#)]
23. Geoffroy, O.; Siebesma, A.P.; Burnet, F. Characteristics of the raindrop distributions in RICO shallow cumulus. *Atmos. Chem. Phys.* **2014**, *14*, 10897–10909. [[CrossRef](#)]
24. Krishna, U.V.M.; Reddy, K.K.; Seela, B.K. Raindrop size distribution of easterly and westerly monsoon precipitation observed over Palau islands in the western Pacific Ocean. *Atmos. Res.* **2016**, *174*, 41–51. [[CrossRef](#)]
25. Hazenberg, P.; Yu, N.; Boudevillain, B.; Delrieu, G.; Uijlenhoet, R. Scaling of raindrop size distributions and classification of radar reflectivity–rain rate relations in intense Mediterranean precipitation. *J. Hydrol.* **2011**, *402*, 179–192. [[CrossRef](#)]
26. Tokay, A.; Short, D.A. Evidence from tropical raindrop spectra of the origin of rain from stratiform versus convective clouds. *J. Appl. Meteor.* **1996**, *35*, 355–371. [[CrossRef](#)]
27. Bringi, V.N.; Chandrasekar, V.; Hubbert, J.; Gorgucci, E.; Randeu, W.L.; Schoenhuber, M. Raindrop size distribution in different climatic regimes from disdrometer and dualpolarized radar analysis. *J. Atmos. Sci.* **2003**, *60*, 354–365. [[CrossRef](#)]
28. Ulbrich, C.W.; Atlas, D. Microphysics of raindrop size spectra: Tropical continental and maritime storms. *J. Appl. Meteor. Climatol.* **2007**, *46*, 1777–1791. [[CrossRef](#)]
29. Joss, J.; Waldvogel, A. Ein Spektrograph für Niederschlagstropfen mit automatischer Auswertung. *Pure Appl. Geophys.* **1967**, *68*, 240–246. [[CrossRef](#)]
30. Löffler-Mang, M.; Joss, J. An Optical Disdrometer for Measuring Size and Velocity of Hydrometeors. *J. Atmos. Ocean. Technol.* **2000**, *17*, 130–139. [[CrossRef](#)]
31. Schönhuber, M.; Lammer, G.; Randeu, W.L. One decade of imaging precipitation measurement by 2D-video-distrometer. *Adv. Geosci.* **2007**, *10*, 85–90. [[CrossRef](#)]
32. Islam, T.; Rico-Ramirez, M.A.; Thurai, M. Characteristics of raindrop spectra as normalized gamma distribution from a Joss-Waldvogel disdrometer. *Atmos. Res.* **2012**, *108*, 57–73. [[CrossRef](#)]
33. Chen, B.J.; Yang, J.; Pu, J.P. Statistical characteristics of raindrop size distribution in the Meiyu season observed in eastern China. *J. Meteor. Soc. Jpn.* **2013**, *91*, 215–227. [[CrossRef](#)]

34. Marzano, F.S.; Cimini, D.; Montopoli, M. Investigating precipitation microphysics using ground-based microwave remote sensors and disdrometer data. *Atmos. Res.* **2010**, *97*, 583–600. [[CrossRef](#)]
35. Chen, B.J.; Hu, Z.Q.; Liu, L.P.; Zhang, G.F. Raindrop size distribution measurements at 4,500 m on the Tibetan Plateau during TIPEX-III. *J. Geophys. Res.* **2017**, *122*, 11092–11106. [[CrossRef](#)]
36. Comstock, K.K.; Wood, R.; Yuter, S.E.; Bretherton, C.S. Reflectivity and rain rate in and below drizzling stratocumulus. *Q. J. R. Meteorol. Soc.* **2004**, *130*, 2891–2918. [[CrossRef](#)]
37. Tokay, A.; Kruger, A.; Krajewski, W.F.; Kucera, P.A.; Filho, A.J.P. Measurements of drop size distribution in the southwestern Amazon basin. *J. Geophys. Res.* **2002**, *107*. [[CrossRef](#)]
38. Atlas, D.; Ulbrich, C.W.; MarksJr, F.D.; Amitai, E.; Williams, C.R. Systematic variation of drop size and radar-rainfall relations. *J. Geophys. Res.* **1999**, *104*, 6155–6169. [[CrossRef](#)]
39. Maki, M.; Keenan, T.D.; Sasaki, Y.; Nakamura, K. Characteristics of the raindrop size distribution in tropical continental squall lines observed in Darwin, Australia. *J. Appl. Meteor.* **2001**, *40*, 1393–1412. [[CrossRef](#)]
40. Reddy, K.K.; Kozu, T. Measurement of rain drop size distribution over Gadanki during south-west and north-east monsoon. *Indian J. Radio Space Phys.* **2003**, *32*, 286–295.
41. Sharma, S.; Konwar, M.; Sarma, D.K.; Kalapureddy, M.C.R.; Jain, A.R. Characteristics of Rain Integral Parameters during Tropical Convective, Transition, and Stratiform Rain at Gadanki and Its Application in Rain Retrieval. *J. Appl. Meteor. Climatol.* **2009**, *48*, 1245–1266. [[CrossRef](#)]
42. Wu, Y.; Liu, L. Statistical characteristics of raindrop size distribution in the Tibetan Plateau and southern China. *Adv. Atmos. Sci.* **2017**, *34*, 727–736. [[CrossRef](#)]
43. Wen, L.; Zhao, K.; Wang, M.Y.; Zhang, G.F. Seasonal variations of observed raindrop size distribution in East China. *Adv. Atmos. Sci.* **2019**, *36*, 346–362. [[CrossRef](#)]
44. Yang, Q.Q.; Dai, Q.; Han, D.W.; Chen, Y.H.; Zhang, S.L. Sensitivity analysis of raindrop size distribution parameterizations in WRF rainfall simulation. *Atmos. Res.* **2019**, *228*, 1–13. [[CrossRef](#)]
45. Brown, B.R.; Bell, M.M.; Frambah, A.J. Validation of simulated hurricane drop size distributions using polarimetric radar. *Geophys. Res. Lett.* **2016**, *43*, 910–917. [[CrossRef](#)]
46. Khain, A.; Lynn, B.; Shpund, J. High resolution WRF simulations of Hurricane Irene: Sensitivity to aerosols and choice of microphysical schemes. *Atmos. Res.* **2016**, *167*, 129–145. [[CrossRef](#)]
47. Kala, J.; Andrys, J.; Lyons, T.J.; Foster, I.J.; Evans, B.J. Sensitivity of WRF to driving data and physics options on a seasonal time-scale for the southwest of Western Australia. *Clim. Dyn.* **2015**, *44*, 633–659. [[CrossRef](#)]
48. Gilmore, M.S.; Straka, J.M.; Rasmussen, E.N. Precipitation uncertainty due to variations in precipitation particle parameters within a simple microphysics scheme. *Mon. Weather Rev.* **2004**, *132*, 2610–2627. [[CrossRef](#)]
49. Chen, F.H.; Yu, Z.C.; Yang, M.L. Holocene moisture evolution in arid central Asia and its out-of-phase relationship with Asian monsoon history. *Quat. Sci. Rev.* **2008**, *27*, 351–364. [[CrossRef](#)]
50. Huang, W.; Chang, S.Q.; Xie, C.L. Moisture sources of extreme summer precipitation events in North Xinjiang and their relationship with atmospheric circulation. *Adv. Clim. Chang. Res.* **2017**, *8*, 12–17. [[CrossRef](#)]
51. Huang, W.; Feng, S.; Chen, J. Physical Mechanisms of Summer Precipitation Variations in the Tarim Basin in Northwestern China. *J. Clim.* **2015**, *28*, 3579–3591. [[CrossRef](#)]
52. Zeng, Y.; Yang, L.M. Triggering Mechanism of an Extreme Rainstorm Process near the Tianshan Mountains in Xinjiang, an Arid Region in China, Based on a Numerical Simulation. *Adv. Meteorol.* **2020**, *2020*. [[CrossRef](#)]
53. Zeng, Y.; Zhou, Y.S.; Yang, L.M. A preliminary analysis of the formation mechanism for a heavy rainstorm in western Xinjiang by numerical simulation. *Chin. J. Atmos. Sci.* **2019**, *43*, 372–388. (In Chinese)
54. Lim, K.-S.S.; Hong, S.-Y. Development of an effective double-moment cloud microphysics scheme with prognostic cloud condensation nuclei (CCN) for weather and climate models. *Mon. Weather Rev.* **2010**, *138*, 1587–1612. [[CrossRef](#)]
55. Thompson, G.; Eidhammer, T. A study of aerosol impacts on clouds and precipitation development in a large winter cyclone. *J. Atmos. Sci.* **2014**, *71*, 3636–3658. [[CrossRef](#)]
56. Zeng, Y.; Yang, L.M. Comparative analysis on mesoscale characteristics of two severe short-time precipitation events in the west of southern Xinjiang. *Torrential Disasters* **2017**, *36*, 410–421. (In Chinese)
57. Liu, L.; Zheng, J. Algorithms for Doppler Spectral Density Data Quality Control and Merging for the Ka-Band Solid-State Transmitter Cloud Radar. *Remote Sens.* **2019**, *11*, 209. [[CrossRef](#)]
58. Battaglia, A.; Rustemeier, E.; Tokay, A. PARISVEL snow observations: A critical assessment. *J. Atmos. Oceanic Technol.* **2010**, *27*, 333–344. [[CrossRef](#)]

59. Testud, J.S.; Oury, S.; Black, R.A.; Amayenc, P.; Dou, X. The concept of “normalized” distribution to describe raindrop spectra: A tool for cloud physics and cloud remote sensing. *J. Appl. Meteor.* **2001**, *40*, 1118–1140. [[CrossRef](#)]
60. Ulbrich, C.W. Natural Variations in the Analytical Form of the Raindrop Size Distribution. *J. Clim. Appl. Meteorol.* **1983**, *22*, 1764–1775. [[CrossRef](#)]
61. Willis, P.T. Functional fits to some observed drop size distributions and parameterization of rain. *J. Atmos. Sci.* **1984**, *41*, 1648–1661. [[CrossRef](#)]
62. Illingworth, A.J.; Blackman, T.M. The need to represent raindrop size spectra as normalized gamma distributions for the interpretation of polarization radar observations. *J. Appl. Meteor.* **2002**, *41*, 286–297. [[CrossRef](#)]
63. Torres, D.S.; Porrà, J.M.; Creutin, J.D. A general formulation for raindrop size distribution. *J. Appl. Meteor.* **1994**, *33*, 1494–1502. [[CrossRef](#)]
64. Kozu, T.; Nakamura, K. Rainfall parameter estimation from dual-radar measurements combining reflectivity profile and path-integrated attenuation. *J. Atmos. Ocean. Technol.* **1991**, *8*, 259–271. [[CrossRef](#)]
65. Lam, H.Y.; Din, J.; Jong, S.L. Statistical and physical descriptions of raindrop size distributions in equatorial Malaysia from disdrometer observations. *Adv. Meteorol.* **2015**, *2015*. [[CrossRef](#)]
66. Li, H.; Yin, Y.; Shan, Y.P. Statistical characteristics of raindrop size distribution for stratiform and convective precipitation at different altitudes in Mt. Huangshan. *Chin. J. Atmos. Sci.* **2018**, *42*, 268–280. (In Chinese)
67. Chen, C.; Yin, Y.; Chen, B.J. Raindrop Size Distribution at Different Altitudes in Mt. Huang. *Trans. Atmos. Sci.* **2015**, *38*, 388–395.
68. Villalobos-Puma, E.; Martinez-Castro, D.; Flores-Rojas, J.L.; Saavedra-Huanca, M.; Silva-Vidal, Y. Diurnal Cycle of Raindrops Size Distribution in a Valley of the Peruvian Central Andes. *Atmosphere* **2020**, *11*, 38. [[CrossRef](#)]
69. Jin, Q.; Yuan, Y.; Liu, H.J.; Shi, C.E.; Li, J.B. Analysis of microphysical characteristics of the raindrop spectrum over the area between the Yangtze River and the Huaihe River during summer. *Acta Meteorol. Sin.* **2015**, *73*, 778–788. (In Chinese)
70. Rosenfeld, D.; Ulbrich, C.W. Cloud Microphysical Properties, Processes, and Rainfall Estimation Opportunities. *Meteorol. Monogr.* **2003**, *30*, 237–258. [[CrossRef](#)]
71. Niu, S.J.; An, X.L.; Sang, J.R. Observational Research on Physical Feature of Summer Rain Dropsize Distribution under Synoptic Systems in Ningxia. *Plateau Meteor.* **2002**, *21*, 37–44. (In Chinese)
72. Moumouni, S.; Gosset, M.; Houngninou, E. Main features of rain drop size distributions observed in Benin, West Africa, with optical disdrometers. *Geophys. Res. Lett.* **2008**, *35*, 23. [[CrossRef](#)]
73. Huang, X.Y.; Yin, J.N.; Ma, L. Comprehensive statistical analysis of rain drop size distribution parameters and their application to weather radar measurement in Nanjing. *Chin. J. Atmos. Sci.* **2019**, *43*, 691–704. (In Chinese)
74. Zhang, A.S.; Hu, J.J.; Chen, S.; Hu, D.M.; Liang, Z.Q.; Huang, C.Y. Statistical Characteristics of Raindrop Size Distribution in the Monsoon Season Observed in Southern China. *Remote Sens.* **2019**, *11*, 432. [[CrossRef](#)]

Publisher’s Note: MDPI stays neutral with regard to jurisdictional claims in published maps and institutional affiliations.



© 2020 by the authors. Licensee MDPI, Basel, Switzerland. This article is an open access article distributed under the terms and conditions of the Creative Commons Attribution (CC BY) license (<http://creativecommons.org/licenses/by/4.0/>).